

The MUSE view of the Sculptor galaxy: survey overview and the planetary nebulae luminosity function.

E. Congiu^{*}¹, F. Scheuermann², K. Kreckel², A. Leroy^{3,4}, E. Emsellem^{5,6}, F. Belfiore⁷, J. Hartke^{8,9,10}, G. Anand¹¹, O. V. Egorov², B. Groves¹², T. Kravtsov^{9,8}, D. Thilker¹³, C. Tovo¹⁴, F. Bigiel¹⁵, G. A. Blanc^{16,17}, A. D. Bolatto¹⁸, S. A. Cronin¹⁸, D. A. Dale¹⁹, R. McClain^{3,4}, J. E. Méndez-Delgado²⁰, E. K. Oakes²¹, R. S. Klessen^{22,23,24,25}, E. Schinnerer²⁶, T. G. Williams²⁷.

(Affiliations can be found after the references)

ABSTRACT

NGC 253, the Sculptor galaxy, is the southern, massive, star-forming disk galaxy closest to the Milky Way. In this work, we present a new 103-pointing MUSE mosaic of this galaxy covering the majority of its star-forming disk up to $0.75 \times R_{25}$. With an area of $\sim 20 \times 5$ arcmin² ($\sim 20 \times 5$ kpc², projected) and a physical resolution of ~ 15 pc, this mosaic constitutes one of the largest, highest physical resolution integral field spectroscopy surveys of any star-forming galaxy to date. Here, we exploit the mosaic to identify a sample of ~ 500 planetary nebulae (~ 20 times larger than in previous studies) to build the planetary nebula luminosity function (PNLF) and obtain a new estimate of the distance to NGC 253. The value obtained is 17% higher than estimates returned by other reliable measurements, mainly obtained via the top of the red giant branch method (TRGB). The PNLF also varies between the centre ($r < 4$ kpc) and the disk of the galaxy. The distance derived from the PNLF of the outer disk is comparable to that of the full sample, while the PNLF of the centre returns a distance ~ 0.9 Mpc larger. Our analysis suggests that extinction related to the dust-rich interstellar medium and edge-on view of the galaxy (the average $E(B - V)$ across the disk is ~ 0.35 mag) plays a major role in explaining both the larger distance recovered from the full PNLF and the difference between the PNLFs in the centre and in the disk.

Key words. Galaxies: individual: NGC 253 – Galaxies: distances and redshifts – planetary nebulae: general – ISM: dust, extinction

1. Introduction

NGC 253, also known as the Sculptor galaxy, is one of the closest ($D \sim 3.5$ Mpc; Newman et al. 2024; Okamoto et al. 2024) massive ($M_{\text{star}} \sim 4.4 \times 10^{10} M_{\odot}$; Bailin et al. 2011; Leroy et al. 2021) star-forming galaxies to the Milky Way. It is also one of the largest galaxies in the sky, with an apparent size of 42×12 arcmin² (Jarrett et al. 2019). With its prominent stellar bar, well-defined spiral arms (Iodice et al. 2014), and star formation spread across the disk, NGC 253 represents a nearby, archetypal example of a main-sequence spiral galaxy.

Its star formation rate (SFR) has been estimated to be between ~ 4.9 (Leroy et al. 2019) and $\sim 6.5 M_{\odot} \text{ yr}^{-1}$ (Jarrett et al. 2019). Almost a third of it ($\sim 2 M_{\odot} \text{ yr}^{-1}$; Bendo et al. 2015; Leroy et al. 2015) is produced by 10 giant molecular clouds distributed in a starburst ring (~ 500 pc in diameter; Leroy et al. 2015) around its nucleus, making this object the closest massive starburst to our Galaxy. In addition, the starburst is responsible for launching a powerful multi-phase outflow (e.g. Strickland et al. 2000; Bauer et al. 2007; Westmoquette et al. 2011; Bolatto et al. 2013; Walter et al. 2017; Lopez et al. 2023; Cronin et al. 2025) that is ejecting large amounts of gas ($14\text{--}39 M_{\odot} \text{ yr}^{-1}$ for the molecular component only, Krieger et al. 2019) from the centre of the galaxy into its circumgalactic medium. Part of this gas seems to remain in the gravitational well of the galaxy, where it cools down to the neutral phase and moves towards the outskirts of the disk (Lucero et al. 2015), potentially reaccreting and fueling future star formation.

The proximity of the galaxy allows for excellent spatial resolution to be achieved even with ground-based telescopes given

the $17 \text{ pc arcsec}^{-1}$ scale. However, when combined with the large intrinsic size of the galaxy (see Table 1), this proximity also results in a large apparent size, causing studies in the last decades to focus mostly on the smaller central structures, such as the starburst (e.g. Bendo et al. 2015; Leroy et al. 2015) and its related outflow (e.g. Strickland et al. 2000; Bauer et al. 2007; Westmoquette et al. 2011; Bolatto et al. 2013; Walter et al. 2017; Lopez et al. 2023).

In this galaxy, we have the possibility to resolve the individual components of the star formation process (giant molecular clouds, H II regions, their ionising sources) for thousands of sources distributed across a wide variety of environments (centre, bar, outflow, spiral arms, inter-arm regions) with a resolution that is a factor of 2–5 better than for most of the latest integral field unit (IFU) surveys of nearby galaxies (e.g., SIGNALS: Rousseau-Nepton et al. 2018; MAD: Erroz-Ferrer et al. 2019; TYPHOON: Grasha et al. 2022; PHANGS-MUSE: Emsellem et al. 2022), and 50–100 times better than the previous generation large IFU surveys (e.g., CALIFA: Sánchez et al. 2012; Husemann et al. 2013; MaNGA: Wake et al. 2017; Bundy et al. 2015; SAMI: Croom et al. 2012).

Large IFU mosaics of extragalactic objects with such high resolution have been obtained so far only for the dwarf galaxies M33 (SIGNALS: Rousseau-Nepton et al. 2019) and for the Magellanic Clouds (Local Volume Mapper: Drory et al. 2024), which sample substantially different properties than those found in a massive system like NGC 253. Additionally, MUSE observed a few nearby galaxies at high resolution, including NGC 7793 (Della Bruna et al. 2020), M83 (Della Bruna et al. 2022), and NGC 300 (McLeod et al. 2021), but with significantly smaller coverage compared to our mosaic of NGC 253. Therefore, while these datasets have comparable, if not better, spatial resolution,

* econgiu@eso.org

they cannot provide the global view needed to connect small-scale processes with the large-scale properties of galaxies such as gas flows, diffuse ionised gas (DIG), or interactions with pristine gas.

Recently, several facilities (e.g., ALMA, Leroy et al. 2021, Oakes et al. in prep.; JWST, McClain et al. in prep., GO2987, PI: Leroy, Congiu, Faesi; HST, Dalcanton et al. 2009, and GO 17809, PI. D. Thilker; MeerKat, Karapati et al. in prep., MKT-20159, PI: Sardone) have invested significant amounts of observing time to map the entire star-forming disk of NGC 253 at the highest possible spatial resolution. In this paper, we present our new MUSE mosaic of NGC 253 offering an unprecedented view of its ionised interstellar medium (ISM). This compilation of multiwavelength data will allow us to explore a wealth of science objectives, starting from the properties, structure, and composition of the multiphase interstellar medium, to the detailed properties of the stellar populations, and the ejection and re-creation cycle powering the star-formation in the galaxy, just to name a few. The mosaic, composed of 103 unique pointings, is the largest contiguous extragalactic mosaic observed by MUSE so far¹. It covers the vast majority of the star-forming disk, with an average resolution of 15 pc (~ 0.85 arcsec PSF FWHM on average).

Here, we focus on testing and validating the data, performing an analysis of the planetary nebulae luminosity function (PNLF) of the galaxy. Planetary nebulae (PNe) are the final evolutionary stage of intermediate-mass stars (e.g., Kippenhahn et al. 2013). During the post-asymptotic giant branch (AGB) phase, these stars eject their outermost layers, creating a gaseous nebula and exposing their core (Osterbrock & Ferland 2006). The high temperature of the core ($\sim 100\,000$ K) results in a hard spectrum that ionises the surrounding gas, creating a PN. For this reason, the (optical) emission spectra of PNe are rich with high ionisation collisionally excited lines and recombination lines (Osterbrock & Ferland 2006). Among them, the strongest one is the [O III] $\lambda 5007$ line, which can account for up to 13% of the total energy emitted by a PN (e.g., Dopita et al. 1992; Ciardullo 2010; Schönberner et al. 2010). Moreover, the ionising source is small, and it produces a limited number of ionising photons. As a consequence, the typical size of a PN is quite small, with the largest reaching a diameter of ~ 1 pc (Acker et al. 1992).

Because of these properties, when observed at extragalactic distances PNe appear as unresolved, [O III] $\lambda 5007$ -bright sources, making them relatively easy to identify in early-type galaxies where virtually all [O III] $\lambda 5007$ emission is produced by PNe. Moreover, their maximum luminosity has been empirically shown to be constant across galaxies and independent of environment and conditions (e.g. Yao & Quataert 2023), to first approximation. This property, combined with the ease of identification, makes PNe ideal candidates for standard candles. In fact, since the late 1980s (Jacoby 1989; Ciardullo et al. 1989), their luminosity function (the PNLF) has been a popular secondary indicator to measure distances of galaxies within 30 Mpc.

Despite this popularity, the distance of NGC 253 has been estimated by PNLF only twice, by Rekola et al. (2005) and Jacoby et al. (2024). The distances do not agree with each other ($3.34^{+0.26}_{-0.38}$ Mpc for Rekola et al. 2005 and $5.4^{+0.3}_{-0.6}$ Mpc for Jacoby et al. 2024), but both are based on limited samples. In this paper, we use our mosaic to identify a new and larger (~ 20 times)

sample of PNe, build the PNLF for NGC 253, and recover an updated independent estimate of the distance of NGC 253.

In Sec. 2 of this paper we describe the observations, the data reduction procedure, and the spectral fitting. Section 3 focuses on the detection, characterisation, and cleaning of the planetary nebulae (PNe) sample, while Sec. 4 describes the fitting of the PNLF and the comparison with the literature findings. Finally, in Sec. 5 we discuss our results and in Sec. 6 we summarise our results. Table 1 lists the properties we assumed for this galaxy throughout the paper.

Table 1. NGC 253 properties assumed throughout the paper.

RA	00h 47m 33.1s ^a
Dec	-25d 17m 18.6s ^a
Position Angle	52.5 ^a
Inclination	76 ^b
R ₂₅	13.5 arcmin (13.5 kpc ^c)

Notes. ^(a) From HyperLEDA (Makarov et al. 2014) ^(b) From McCormick et al. (2013) ^(c) Assuming a distance of 3.5 Mpc (Okamoto et al. 2024)

2. Observations and data processing

Most of the data presented in this work were acquired as part of ESO programme 108.2289 (P.I. Congiu). We used MUSE in its seeing-limited wide-field mode configuration and with the extended wavelength range (WFM-NOAO-E), which covers between 4600 and 9300 Å with a resolution $R \sim 2000$ at $H\alpha$. The observations were organised in blocks of 2 pointings with three interleaved 120 s sky offset exposures: one at the beginning of each observing block, one between the two pointings, and one at the end. We observed four 211 s exposures per pointing (844 s in total), rotating the field by 90 degrees between each exposure to minimise instrumental signatures in the final mosaic. We originally planned for 98 pointings, covering an approximate area of 20×5 arcmin². However, three pointings were re-observed because of issues with their positioning, resulting in a final total of 101 pointings and ~ 51.5 hours of observing time.

The mosaic also includes two archival pointings observed as part of the ESO programme 0102.B-0078 (P.I. Zschaechner). These data were acquired with MUSE in its seeing-enhancing ground-layer adaptive optics wide-field mode configuration and with the extended wavelength range (WFM-AO-E), covering the same wavelength range as our original data. Each pointing has been observed with four 490 s exposures (1960 s in total), with 90-degree field rotations and small offsets between exposures. Two 125 s sky exposures were also acquired using a typical OSOOSO offset pattern. The main differences between these archival data and ours are the longer exposure times and a masked spectral region between 5760 and 6010 Å, introduced to avoid laser contamination. Table B.1 summarises the main properties of the observations, such as date, average airmass, average seeing, and full width at half maximum (FWHM) of the PSF at 5000 Å, recovered as described in Sec. 3.2.

The final mosaic covers an area of $\sim 20 \times 5$ arcmin² ($\sim 20 \times 5$ kpc² at the distance of the galaxy, projected), extending roughly out to $0.75 \times R_{25}$. This corresponds to ~ 9 million spectra and a final file size of ~ 300 GB. Figure 1 shows the reduced mosaic. The top panel shows a colour image produced by combining g-, r-, and i-band images extracted from the datacube. The

¹ The absolute largest MUSE mosaic is the Large Magellanic Cloud one published in Boyce et al. (2017) and it covers 1 deg² with a filling factor of 25%. Other large mosaics of Milky Way structures are available in the MUSE archive, although they have not been published yet.

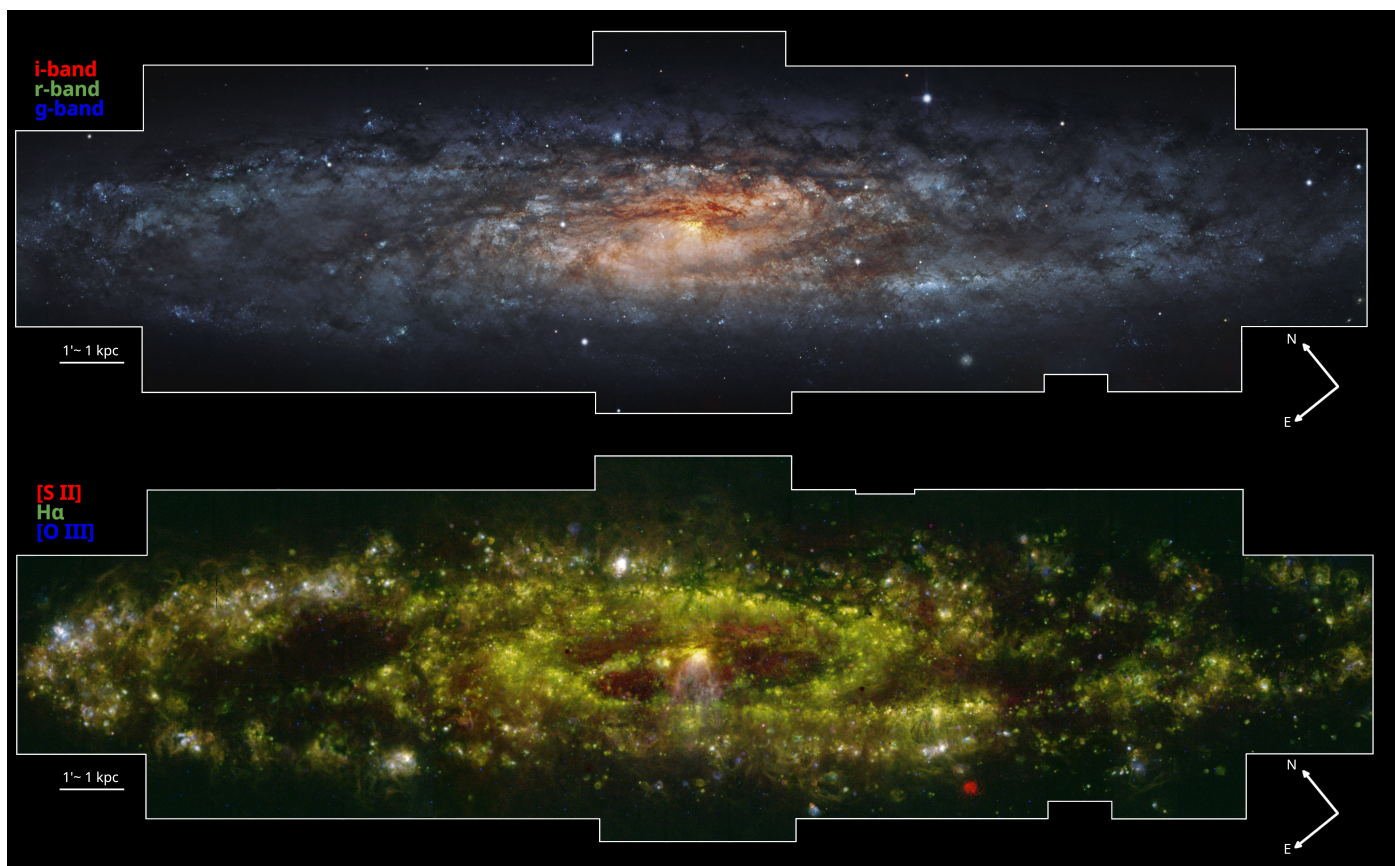


Fig. 1. Colour images of NGC 253 produced by combining broad-band images and emission line maps extracted from the MUSE data cube. The mosaic covers an area of 20×5 arcmin² and it includes roughly 9 million independent spectra. The top panel shows a composition of three broad-band filters: g-band in blue, r-band in green, and i-band in red (Acknowledgement: ESO/M. Kornmesser). We can see the full structure of the galaxy disk, with the prominent bar and complex dust filaments that follow the distribution of the spiral arms of the galaxy. We can also see the change in colour caused by the presence of the central starburst of the galaxy. The bottom panel is a composition of emission line maps with [O III]λ5007 in blue, Hα in green and [S II]λλ6717, 6731 in red. This highlights the multitude of ionised gas structures we observe in the galaxy. The H II regions distribution highlights the structure of the spiral arms, while the [O III]λ5007 and [S II]λλ6717, 6731 emission clearly show the outline of the outflow. Nebulae with different properties can be identified across the field, like the blue, [O III]λ5007 emitting PNe, the green Hα bright H II regions, and the pink, [S II]λλ6717, 6731 emitting SNRs.

bottom panel highlights the gas emission, showing [O III]λ5007, Hα, and [S II]λλ6717, 6731.

2.1. Data reduction

All data have been reduced using `pymusepipe`, a python wrapper of the ESO MUSE pipeline (Weilbacher et al. 2020) presented in Emsellem et al. (2022). The reduction procedure follows the one described for the PHANGS-MUSE data in the latter work. However, there are some significant differences that we highlight in the following paragraphs.

2.1.1. Alignment

The astrometry provided by the MUSE pipeline is not accurate enough for combining multiple exposures into a large mosaic. Emsellem et al. (2022) addressed this by manually aligning each exposure to a reference R-band image from the PHANGS-Hα survey (Razza et al. in prep.). They extracted broad-band images from the MUSE cubes using the PHANGS-Hα filter transmission curve, and aligned them by applying sub-pixel shifts and rotations to match the reference image.

While effective, this method is time consuming and somewhat subjective. We instead used a semi-automatic routine based

on the `spacepylot` package², which employs optical flow to determine alignment corrections. This technique compares two images of the same object and computes the vector field required to transform one into the other. `spacepylot` then averages these vectors to derive global shifts and rotations, which we applied to individual exposures following Emsellem et al. (2022).

NGC 253 was not part of the PHANGS-Hα survey, but several WFI R-band images are publicly available in the ESO archive. We reduced them using the pipeline of Razza et al. (in prep.) and Emsellem et al. (2022), and used the resulting R-band mosaic as our astrometric reference. This image was aligned to Gaia DR2 (Gaia Collaboration et al. 2018; Lindegren et al. 2018). Comparing stellar positions in the WFI image with Gaia, we found astrometric offsets of 0.02 ± 0.60 arcsec in RA and 0.03 ± 0.46 arcsec in Dec.

2.1.2. Sky subtraction

The sky subtraction is the most critical step in this data reduction. When observing extended targets with MUSE, the typical strategy is to regularly observe an empty sky field close to the target.

² <https://github.com/ejwatkins-astro/spacepylot>

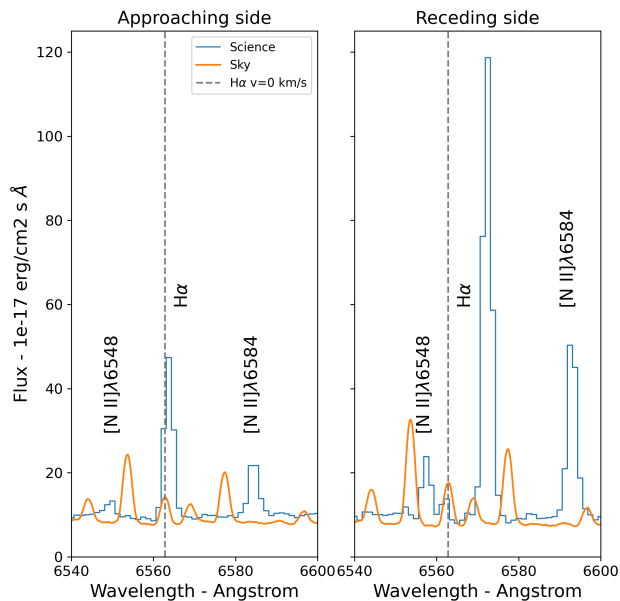


Fig. 2. $H\alpha$ region of the spectra in two different regions of the galaxy. The left panel represent the approaching side of the galaxy, while the right panel the receding side. In both panels we show in blue the spectrum extracted from the science exposure after our updated sky subtraction procedure, in orange the sky spectrum associated with the exposure, while the grey dashed lines represent the expected position of $H\alpha$ at $v = 0$ km/s.

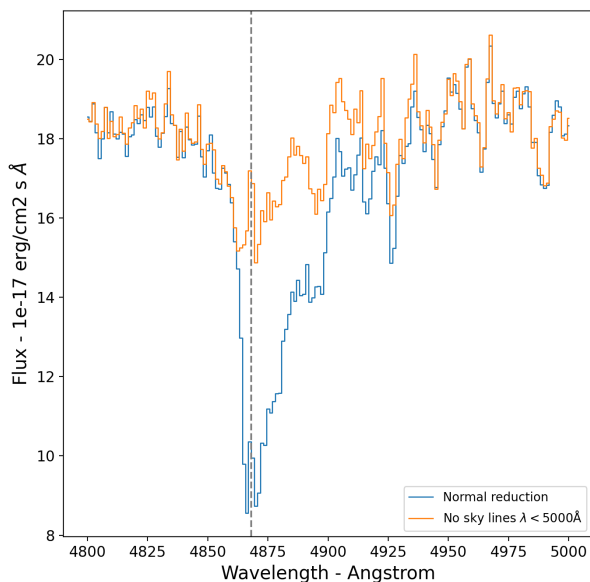


Fig. 3. $H\beta$ region of the spectra in a 4 arcsec circular aperture extracted from one of the pointings with an asymmetric $H\beta$ profile. The blue line represents the spectrum obtained from the normal sky subtraction, while the orange line shows the spectrum obtained after removing the sky lines with wavelengths shorter than 5000 Å from the line list used to build the sky model from the dedicated sky offset. The vertical, dashed, grey line, represents the expected position of the $H\beta$ emission line, considering the rotation curve of the galaxy.

The MUSE pipeline’s standard sky subtraction routine³ (Weilbacher et al. 2020) uses these sky exposures to build a model of the sky emission, separating it into continuum and emission-line components. The continuum component is directly subtracted from the science exposures. Emission lines, instead, are grouped by physical origin, compared to the faintest spaxels in the science frames, re-scaled, and then subtracted. This allows for improved sky subtraction, especially considering that some of these line groups (e.g. [O I], OH) vary significantly on short timescales and can result in significant artefacts if not treated carefully.

This strategy works well for most extragalactic targets, which typically have a significant redshift. NGC 253, however, is a very local source, with a systemic line-of-sight velocity of $v_{\text{sys}} \sim 242$ km s⁻¹ and a rotation curve of ± 200 km s⁻¹ (Hlavacek-Larrondo et al. 2011). This means that the approaching side of the galaxy has a relative velocity of only ~ 40 km s⁻¹, and that some of the target’s lines fall very close to their atmospheric counterparts (Fig. 2). Since this velocity difference is just below the instrument resolution of ~ 50 km s⁻¹ at $H\alpha$, the pipeline cannot reliably separate sky and target emission, resulting in the over-subtraction of such lines unless they are not tied to a larger group. This issue affects mostly the [O I] lines (especially [O I] λ 6300, [O I] λ 6363, and [O I] λ 5577) and the hydrogen Balmer lines ($H\alpha$ and $H\beta$). While the [O I] lines are among the most variable in the night sky (produced by atmospheric atoms excited through collisions with charged particles; Bates 1946; Solomon et al. 1988), the Balmer lines are more stable (caused by high-atmosphere hydrogen excited by solar Ly α ; Nossal et al. 2019). Because their intensity varies slowly on the 5–10 minute scale between sky and object exposures, the Balmer lines can be treated as constant during this interval. This is especially important as they are two of the most important lines in the ionised gas spectrum, and their slow rate of change allow us to recover their flux from the dedicated sky exposures and subtract it directly from the science frames. To enable this, we excluded $H\alpha$ and $H\beta$ from the pipeline’s list of fitted sky emission lines, forcing them to be treated as part of the continuum.

In addition, we identified several pointings with an asymmetric and unphysical $H\beta$ absorption profile (Fig. 3). This was an artefact caused by the overfitting of sky lines near the $H\beta$ region. Since the Paranal sky spectrum does not contain bright lines at $\lambda < 5000$ Å (Hanuschik 2003), we solved the issue by excluding all sky lines bluer than 5000 Å from the pipeline’s list. This removed ~ 9000 lines, almost 40% of the full list. Figure 3 shows a comparison between the original spectrum (blue) and the corrected one (orange). Although not all exposures are affected by these issues, we applied the improved sky subtraction procedure to the entire dataset for consistency. We then combined all reduced exposures into the final mosaic following the method of Emsellem et al. (2022).

2.2. Spectral fitting

We processed the data with the PHANGS data analysis pipeline (DAP) to compute the properties and kinematics of the underlying stellar population, subtract their continuum from the spectra, and extract the flux of the main emission lines. The DAP is described in detail in Emsellem et al. (2022), but here we summarise the main features relevant to this work. The DAP runs the spectral fitting routine, based on the ppxf package (Cappellari 2017), three times. The first run is performed on Voronoi-binned data using a reduced set of simple stellar population models from

³ skymethod=model in the scipost options.

Table 2. Summary of the PNe candidates identified in the paper.

Sample	Triple	Double	Single	Total
E.C.	444	105	42	591
C.T.	444	95	163	702
T.K.	444	74	46	564
Final	444	137	251	832

Notes. The columns show: the name of the sample (indicated by the initials of the person who created the sample for the original catalogues), the number of objects in common to the three catalogues, the number of objects included in two catalogues, the number of objects identified by a single catalogue, and the number of objects in total.

the E-MILES library (Vazdekis et al. 2016) to characterise the stellar kinematics across the galaxy. The second run uses the same Voronoi-binned spectra, keeps the kinematics fixed from the first step, and employs a more extensive library of simple stellar population models (also from the E-MILES library Vazdekis et al. 2016) to extract additional stellar population parameters (e.g., age, metallicity). Finally, a third run is performed on each individual spaxel to remove the stellar continuum and simultaneously fit the emission lines with Gaussian profiles. The kinematics of the stellar templates is fixed from the first step, and the reduced template sample is used for the fit. Emission lines are grouped into three sets with fixed kinematics (see Sec. 5.2.5 of Emsellem et al. 2022). At the end of the process, the final results are compiled in a multi-extension FITS file, the MAPS file, which contains two-dimensional maps of all fitted parameters. The physical quantities in the output files are summarised in Tab. B.4, while Tab. B.3 lists the emission lines included in the fit.

We also extract moment-zero, -one, and -two maps of the main emission lines to recover more complete flux and kinematics information in regions where the DAP’s single-Gaussian fit is insufficient to represent the real line profile (e.g., the galaxy centre). All maps were extracted from continuum-subtracted cubes produced by the DAP using an extraction window of $\pm 500 \text{ km s}^{-1}$ around the recession velocity of the galaxy. The only exception is the $[\text{S II}]\lambda\lambda 6717, 6731$ doublet, for which we used a larger extraction window ($\pm 750 \text{ km s}^{-1}$) centred on the average wavelength of the two lines, to avoid cross-contamination. For these lines, we recovered only the moment-zero map and its associated error map.

3. Analysis

In this section, we present the analysis we performed to identify, characterise, and clean from contaminants the sample of PNe that we used to build the PNLF and estimate the distance of NGC 253.

3.1. Detection of the planetary nebulae candidates

PNe in galaxies outside the local group appear as $[\text{O III}]\lambda 5007$ -bright point sources due to their small physical size ($< 1 \text{ pc}$, e.g., Acker et al. 1992) and the high degree of ionisation of their gas. As a result, all common PNe identification techniques, such as image “blinking” (e.g., Jacoby 1989), automatic point source detection (e.g., Scheuermann et al. 2022), colour-magnitude diagram analysis (Arnaboldi et al. 2002), or differential emission-line filtering (Roth et al. 2021), focus on analysing $[\text{O III}]\lambda 5007$ emission line maps in various forms.

We detect our PNe candidates using a visual approach based on the $[\text{O III}]\lambda 5007$, $\text{H}\alpha$, and $[\text{S II}]\lambda\lambda 6717, 6731$ moment maps (Fig. 4). We used both an RGB image combining the three maps (blue for $[\text{O III}]\lambda 5007$, green for $\text{H}\alpha$, and red for $[\text{S II}]\lambda\lambda 6717, 6731$) and the individual $\text{H}\alpha$ and $[\text{O III}]\lambda 5007$ maps. We first selected as PNe candidates all sources in the $[\text{O III}]\lambda 5007$ map that appeared point-like and lacked a bright counterpart in the $\text{H}\alpha$ map. The RGB map was then used to clarify borderline cases, such as PNe near bright H II regions or objects with detectable $\text{H}\alpha$ emission but still appearing bluer than typical H II regions. The colour map clearly highlights PNe as blue dots even in crowded areas or when their emission is faint and hard to identify in the $[\text{O III}]\lambda 5007$ map. Ambiguous sources were included in the catalogue, relying on the methods in Sec. 3.4 for potential rejection via a quantitative approach. We removed from the catalogue all sources for which reliable $[\text{O III}]\lambda 5007$ photometry was not possible, either due to proximity to other $[\text{O III}]\lambda 5007$ -emitting sources (mainly other PNe candidates) or location at the edge of the mosaic.

We also tested an alternative detection method based on DAOFIND (Stetson 1987), successfully used by other authors under similar conditions (e.g., Scheuermann et al. 2022). This algorithm is quick and semi-automatic but assumes a uniform PSF across the FOV, which is not the case here (see Sec. 3.2), and cannot exploit colour information as effectively as visual inspection. We applied the `photutils` (Bradley et al. 2024) implementation of DAOFIND to the $[\text{O III}]\lambda 5007$ moment-zero map to generate an alternative PNe candidates list. We tried several combinations of the main parameters (thresholds, FWHM, sharpness, and roundness), but none yielded satisfactory results. The software was detecting ~ 10000 objects, which visual inspection showed to be spurious detections or bright spots clearly associated with H II regions. Even after removing contaminants (as described in Sec. 3.4), more than half of these sources were still identified as PNe. We therefore opted to continue the analysis using the visually compiled catalogue. Appendix A discusses the results of the PNLF using the DAOFIND-based catalogue.

However, visual detection can be subjective, and the final candidate list may vary depending on who performs the selection. To reduce this bias, three co-authors (E.C., C.T., and T.K.) independently carried out the detection procedure. Their catalogues were merged into a single compilation. Duplicates were removed by comparing coordinates, merging sources close enough to likely be the same object. We then conducted a second check for sources near each other that might cross-contaminate their photometry. The final catalogue includes 832 PNe candidates. Table 2 summarises its composition and that of each person’s original sample.

3.2. Point spread function

To obtain reliable photometry of our sources, we need a good characterisation of the point spread function (PSF) of the data. It is essential to both select an adequate aperture for the photometry and apply a precise aperture correction. However, NGC 253 observations were performed using ~ 53 OBs (including archival ones) that were acquired between 2018 and 2022 under a wide variety of sky conditions (Table B.1). As a result, the PSF can change significantly across the mosaic.

A common way to characterise the PSF of astronomical data is to fit bright sources across the FOV of the instrument with a model of the PSF. Unfortunately, only a handful of OBs included bright foreground stars that could be used to reliably characterise it, so we devised an alternative method. Given their properties,

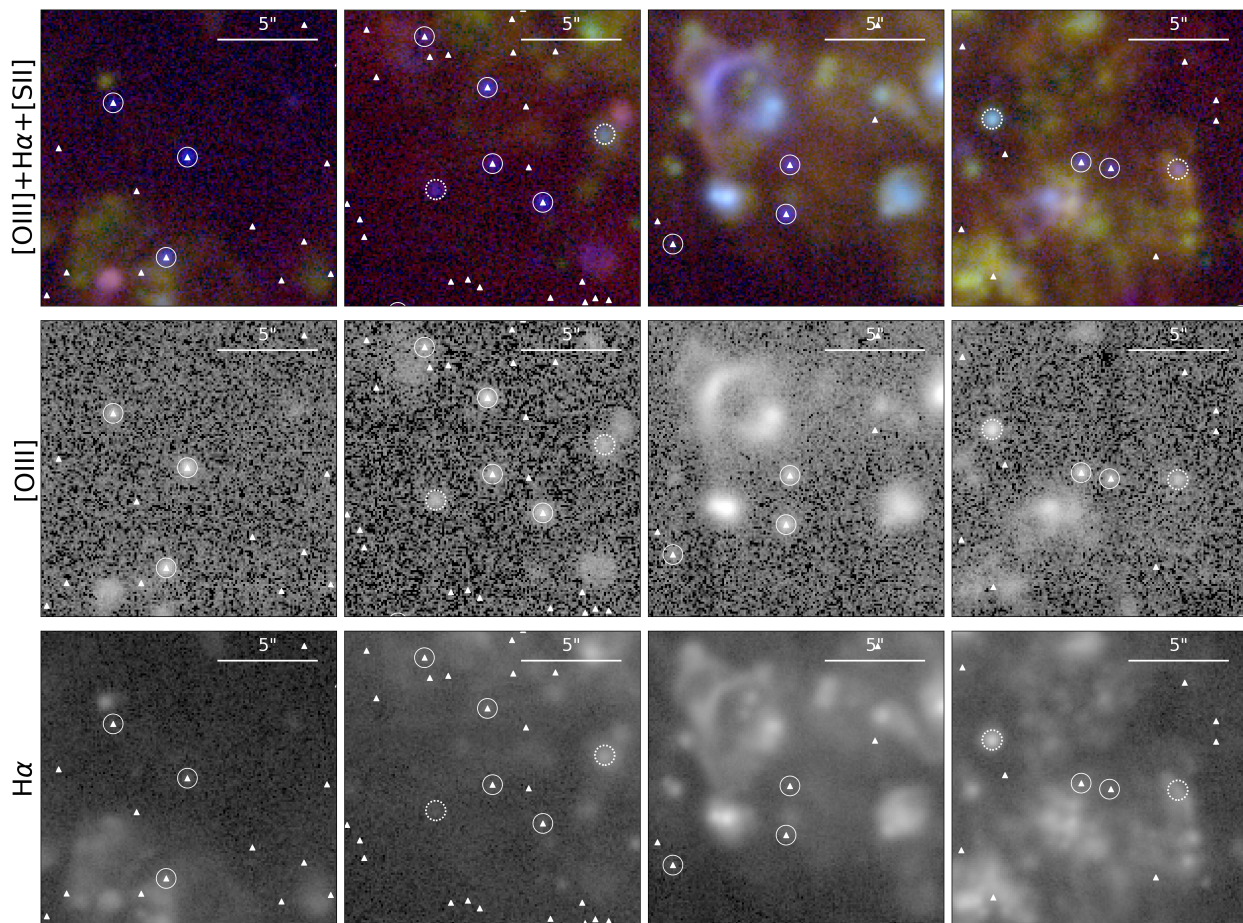


Fig. 4. Example of the different images used for the visual detection of nebulae. We show zoom-ins of four different areas of the galaxy. For each region, we show on the top the three colour map (same colours as in Fig 1, bottom panel), in the middle the $[\text{O III}]\lambda 5007$ and in the bottom the $\text{H}\alpha$ map. The circles highlight the position of nebulae in the final catalogue, with the solid circles showing the position of confirmed PNe and dotted ones showing nebulae classified either as supernova remnants or as compact H II regions. White triangles show the position of the objects identified by DAOFIND, which are, for the most part, spurious detections.

PNe are ideal for characterising the local PSF. They are faint, but the shape of the MUSE-WFM PSF is relatively well studied, and this “a priori” knowledge can be used to decrease the number of free parameters and improve fit reliability. In particular, the PSF can be modelled quite well by a circular Moffat profile (Moffat 1969), characterised, to the first approximation, by a constant power index (2.8 for the NOAO mode and 2.3 for the AO mode Hartke et al. 2020; Emsellem et al. 2022) and variable full width at half maximum (FWHM).

We fitted each PN candidate identified in Sec. 3 with a circular Moffat profile with fixed power index and recovered their FWHM, which we include in the catalogue of PNe candidates available through Vizier. The fit was performed using the $[\text{O III}]\lambda 5007$ moment zero map. In the following analysis, we consider their FWHM as the FWHM of the local PSF at $\sim 5007 \text{ \AA}$, the wavelength of the $[\text{O III}]\lambda 5007$ emission line.

Finally, we take the clean sample of PNe described in Sec. 3.4 to estimate the average FWHM of each pointing in which at least one confirmed PNe is present. We used the clean sample to ensure only confirmed point sources are considered. We report the estimates in Tab. B.1. The average PSF FWHM of our observations is therefore 0.8 arcsec (measured from 100 individual pointings), which corresponds to 13.5 pc, with a standard deviation of 0.2 arcsec. The maximum FWHM is 1.6 arcsec (27 pc) and the minimum is 0.49 arcsec (8.5 pc).

3.3. Aperture photometry

We use photutils to perform aperture photometry of our candidates using moment-zero maps of several emission lines: $[\text{O III}]\lambda 5007$ to build the PNLF, and $\text{H}\alpha$, $[\text{N II}]\lambda 6584$, and $[\text{S II}]\lambda\lambda 6717, 6731$ to reject contaminants (H II regions, SNRs) in the sample. We adopted apertures with diameters equal to the FWHM of the local PSF (see Sec. 3.2). Then, we estimate the local background emission in an annulus with an inner diameter of $4\times\text{FWHM}$ and an area of five times that of the central aperture. To remove the flux component caused by the diffuse emission of the galaxy, we rescaled this background for the difference in size between apertures and subtracted it from the integrated fluxes of the objects. Since the apertures we adopted are small, we leveraged the FWHM of the local PSF to calculate the appropriate aperture correction for each PN⁴. The PSF fit was performed on the $[\text{O III}]\lambda 5007$ moment-zero map, so we adjust the correction according to the wavelength of the considered line to account for the PSF size’s wavelength dependence (as described in Emsellem et al. 2022).

We then corrected for Galactic extinction, using a Cardelli et al. (1989) extinction law with $R(V) = 3.1$ and an $E(B - V)$ of 0.0165 (Schlafly & Finkbeiner 2011). We did not correct for

⁴ We assume the aperture correction reported in Eq. 3 of Scheuermann et al. (2022).

internal extinction, for the reasons we discuss in Sec. 5.4. Finally, we converted the $[\text{O III}]\lambda 5007$ fluxes (in $\text{erg cm}^{-2} \text{s}^{-1}$) to apparent magnitudes using the following equation from [Jacoby \(1989\)](#):

$$m_{5007} = -2.5 \cdot \log_{10} I_{5007} - 13.74 . \quad (1)$$

We estimated errors on the integrated fluxes using the moment-zero error maps and standard error propagation. We also add in quadrature a 0.11 mag error on the $[\text{O III}]\lambda 5007$ magnitudes, which we estimate as the typical uncertainty on the aperture correction from our analysis in Sec. 5.1.

3.4. Contaminants

The next step is to clean our sample of PNe candidates from contaminants. This is particularly important in a star-forming galaxy like NGC 253 where PNe are a minority of the $[\text{O III}]\lambda 5007$ -emitting sources. The two most common contaminants are supernova remnants (SNR) and compact H II regions. To remove them from our catalogue, we leverage the different spectral properties of the three classes of sources. H II regions and PNe are both powered by photoionisation, but the former are ionised by O or B stars that produce a soft ionising spectrum with respect to the white dwarfs typically powering PNe. For H II regions, this results in a spectrum dominated by hydrogen recombination lines ($\text{H}\alpha$ in particular) and other lines from moderately low ionisation ions (e.g., $[\text{N II}]$). Planetary nebulae spectra, on the other hand, are dominated by highly ionised forbidden lines, like $[\text{O III}]\lambda 5007$, and recombination lines, such as $\text{He II} \lambda 685$. Finally, supernova remnants are mostly powered by shocks, which enhance low-ionisation lines like the $[\text{O I}]\lambda 6300$ and $[\text{S II}]\lambda \lambda 6717, 6731$ doublets.

Several methods have been developed in the literature to take advantage of these properties to classify these nebulae. Here, we exploit the two most common. To reject H II regions, we leverage the criterion developed by [Ciardullo et al. \(2002\)](#) and [Herrmann et al. \(2008\)](#):

$$\log_{10} \frac{I_{5007}}{I_{\text{H}\alpha + [\text{N II}]\lambda 6583}} > -0.37 M_{5007} - 1.16 , \quad (2)$$

while for SNRs we apply the traditional [D’Odorico et al. \(1980\)](#) criterion:

$$\log_{10} \frac{I_{[\text{S II}]\lambda 6717 + [\text{S II}]\lambda 6731}}{I_{\text{H}\alpha}} > -0.4 . \quad (3)$$

[Kopsacheili et al. \(2020\)](#) and [Li et al. \(2024\)](#) showed how an $[\text{O I}]\lambda 6300$ based criterion is more effective at identifying SNRs from H II regions. However, the $[\text{O I}]\lambda 6300$ line in our data is heavily compromised by sky emission and we are not interested in a clean sample of SNRs, so we stuck with the criterion in Eq. 2. During the classification, we consider the flux of non-detected lines equal to its uncertainty. We also checked for over-luminous sources, that is, sources that look like PNe but that are significantly brighter than the bright cutoff of the PNLF ([Longoardi et al. 2013](#); [Hartke et al. 2017](#); [Roth et al. 2021](#); [Scheuermann et al. 2022](#)), without finding any of them in our sample. Finally, we exploited the size recovered in the previous section, to reject five objects that are either too large ($\text{FWHM} > 2$ arcsec) or too small ($\text{FWHM} < 0.2$ arcsec). The first criterion rejects extended sources, since all our data were acquired with seeing ~ 1.2 arcsec or better. The second one rejects bad pixels and similar artefacts that can be confused with real sources at first glance.

After all these checks, our clean sample of PNe includes 571 objects. Figure 5 shows the position of the confirmed PNe in the $[\text{O III}]\lambda 5007$ emission line map. Of the remaining 253 regions (without counting the 5 regions rejected for their size), 200 are classified as H II regions, while 53 as SNRs. The catalogue of sources, which contains all the information reported in Table B.2, is available through CADC and Vizier.

4. The planetary nebula luminosity function in NGC 253

The PNLF, that is, the number of PNe observed as a function of their $[\text{O III}]\lambda 5007$ luminosity, is commonly described by an empirical relation, an exponential distribution truncated at the bright end ([Ciardullo et al. 1989](#)):

$$N(M_{5007}) \propto e^{0.307 M_{5007}} \left(1 - e^{3(M_{5007}^* - M_{5007})} \right) , \quad (4)$$

where M_{5007}^* denotes the absolute $[\text{O III}]\lambda 5007$ magnitude of the brightest possible PN, i.e., the zero-point of the luminosity function. Its value is calibrated using galaxies with distances known from primary indicators such as Cepheids or the Tip of the Red Giant Branch (TRGB).

Typical estimates place M_{5007}^* around -4.5 mag, with -4.54 mag from [Ciardullo \(2013\)](#) being the most widely adopted. While a mild metallicity dependence has been reported (e.g., [Ciardullo et al. 2002](#); [Bhattacharya et al. 2021](#); [Scheuermann et al. 2022](#)), its significance remains uncertain. Given that NGC 253 has near-solar metallicity ($12 + \log(\text{O}/\text{H}) = 8.69$; [Beck et al. 2022](#)), where the empirical metallicity dependence is nearly flat, we ignore this dependence and consider $M_{5007}^* = -4.54$ mag throughout our analysis.

We fit Eq. 4 to our data using the maximum likelihood approach of [Scheuermann et al. \(2022\)](#). Figure 6 shows the resulting PNLF (left) and its cumulative form (right). To avoid incompleteness effects at the faint end, we impose a magnitude cutoff based on visual comparison of three independently compiled PN samples (E.C., T.K., C.T.). Figure 7 shows that all three samples begin to drop at ~ 25.5 mag. While a real decline in PN counts is expected ~ 2 mag below the bright end (e.g., [Jacoby & De Marco 2002](#); [Reid & Parker 2010](#); [Ciardullo 2010](#); [Rodríguez-González et al. 2015](#); [Bhattacharya et al. 2021](#)), our model does not account for this feature. We therefore restrict the fit to the 320 PNe brighter than 25.5 mag. The fit returns a distance modulus of $28.07^{+0.04}_{-0.05}$ mag ($4.10^{+0.07}_{-0.09}$ Mpc).

Figure 8 compares the distance from our analysis to previous results from the literature. Our measurement, shown as a solid black vertical line, is accompanied by shaded regions indicating the 1σ (dark grey) and 3σ (light grey) uncertainties. It stands out as significantly larger than most previously reported values. The commonly accepted distance to NGC 253 is ~ 3.5 Mpc, with the most recent estimates reported by [Newman et al. \(2024\)](#) and [Okamoto et al. \(2024\)](#) via TRGB analysis. Our measurement exceeds this value by ~ 0.35 mag (0.6 Mpc), with only two similar distances found in [Willick et al. \(1997\)](#), based on IRAS satellite data and the Tully-Fisher relation ([Tully & Fisher 1977](#)). Among the compiled distances, we have two other measurements via the PNLF: [Rekola et al. \(2005\)](#) and [Jacoby et al. \(2024\)](#). In the following, we will directly compare our result with those two studies.

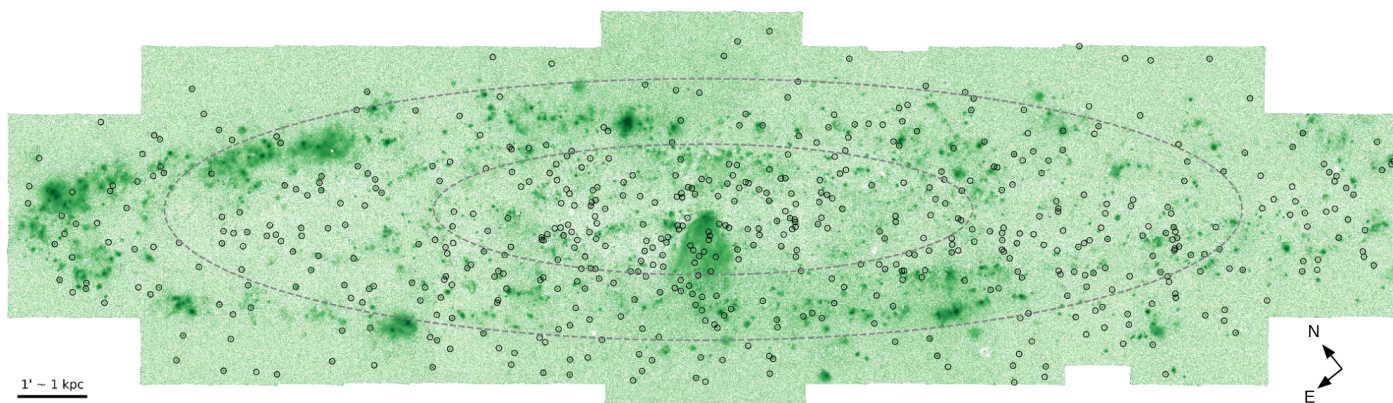


Fig. 5. $[\text{O III}]\lambda 5007$ line map of NGC 253. Empty circles mark the location of confirmed PNe. The grey dashed ellipses represent the boundary used to define the radial bins presented in Sec. 5.2.

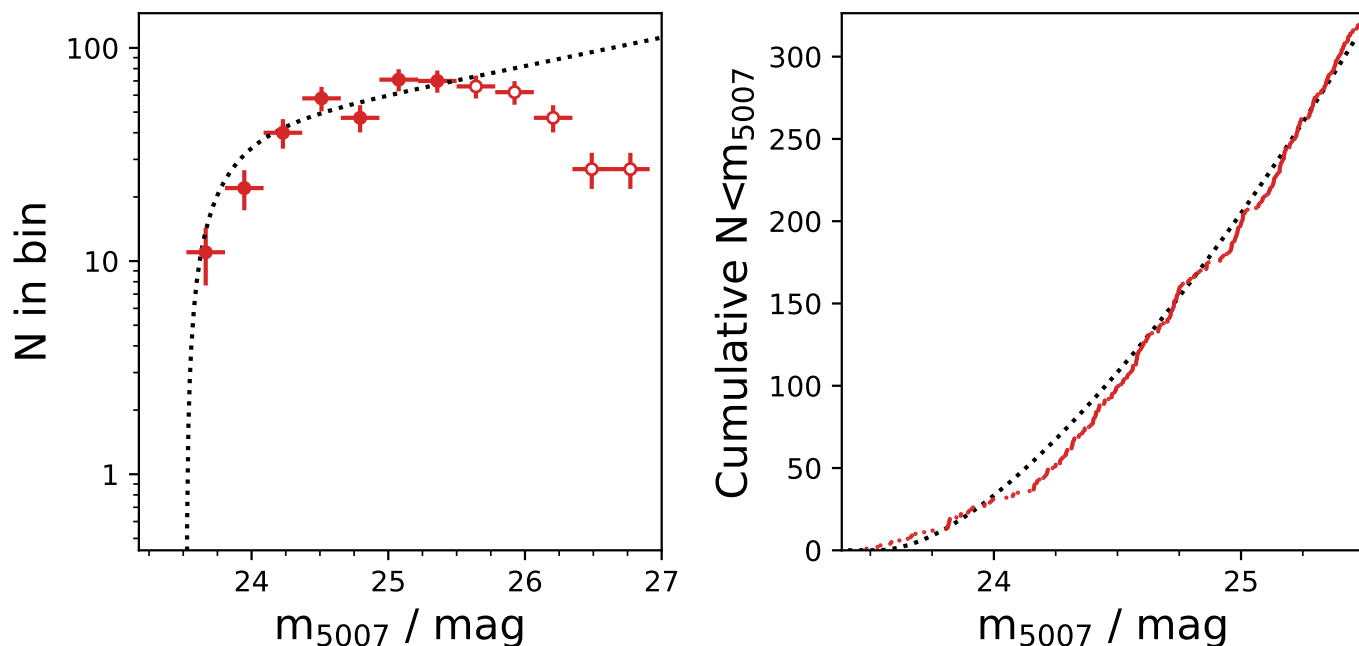


Fig. 6. PNLF and cumulative PNe $[\text{O III}]\lambda 5007$ luminosity function for NGC 253. The red points show the measured PNLF and cumulative function, while the black dashed line represents the best fit model. Empty points mark the bins of the PNLF not considered in the fit.

4.1. Comparison with [Rekola et al. \(2005\)](#)

[Rekola et al. \(2005\)](#) were the first to measure the distance of NGC 253 using the PNLF method through ground-based $[\text{O III}]\lambda 5007$ and $\text{H}\alpha$ narrow-band images acquired with FORS. Of the 24 PNe they detected, they selected the 14 brightest ones for the PNLF fit and obtained a distance of $27.62^{+0.16}_{-0.26}$ mag ($3.34^{+0.26}_{-0.38}$ Mpc). Of these 14 PNe, 12 have counterparts in our sample⁵. We classify all of them as PNe, except one, the brightest in the [Rekola et al. \(2005\)](#) sample, that we classify as an H II region.

The blue circles in Fig. 9 show the difference between our photometry and [Rekola et al. \(2005\)](#), with solid markers denoting the sources used in their PNLF fit and open circles indicating the ones they excluded but that are within our mosaic. Their Milky Way extinction correction slightly differs from ours. To

⁵ Of the two missing objects the first is outside of our mosaic, while the second is not in our sample because of its extended morphology in the MUSE data.

ensure consistency in the comparison, we recalculated our extinction correction using $E(B-V) = 0.019$, $R_V = 3.07$, and a [Fitzpatrick \(1999\)](#) extinction law. There is a scatter of 0.4 mag between the two works, but without a significant offset (0.06 mag). This implies that there is no systematic difference between the two sets of measurements. The observed scatter may be related to the different observing techniques and the inherent challenge of obtaining precise photometry for dim objects against a complex background emission, such as that present in NGC 253.

To confirm that the difference in photometry does not influence the distance of the galaxy, we perform the fit of the PNLF using only the 12 sources in common between the two samples. We measure a distance modulus of $27.38^{+0.14}_{-0.30}$ mag ($3.00^{+0.19}_{-0.42}$ Mpc). This value is slightly smaller, but still within the error bars of [Rekola et al. \(2005\)](#) original measurement, confirming that the difference in photometry is not the cause of the discrepancy. However, we highlight that we include in this fit the object we classify as an H II region. Given the small number of PNe, the PNLF distance is particularly sensitive to the mag-

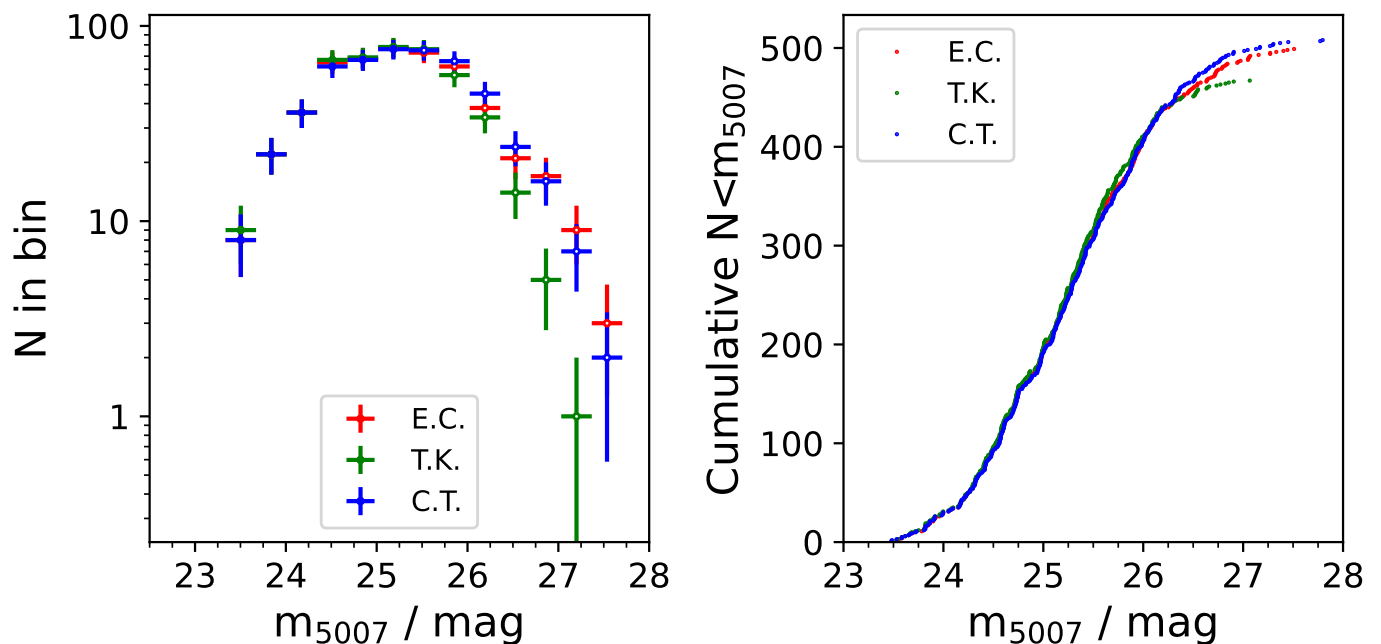


Fig. 7. Comparison between the luminosity functions obtained from the three individual samples described in Sec. 3.1. The left panel shows the PNLFs, while the right panel shows the cumulative luminosity function. The figure shows how the three samples significantly overlap at the bright end, while the number of PNe drops in all cases around 25.5 mag.

nitude of the brightest objects, and this nebula is significantly brighter than the second brightest one in both samples (0.34 mag according to [Rekola et al. 2005](#) photometry and 0.77 mag according to our photometry). Therefore, we repeated the analysis removing this object from the sample, obtaining a distance modulus of $28.02^{+0.12}_{-0.29}$ mag ($4.01^{+0.21}_{-0.54}$ Mpc). Although the errors are large, the value is consistent with what we recover from the full sample, confirming that the discrepancy between our results and those reported in [Rekola et al. \(2005\)](#) is mainly driven by the misclassification of this single object.

4.2. Comparison with [Jacoby et al. \(2024\)](#)

[Jacoby et al. \(2024\)](#) recently estimated the distance of NGC 253 via the PNLF using the two archival MUSE pointings from programme 0102.B-0078 (P.I. Zschaechner). Their analysis employs the differential emission line filter method introduced by [Roth et al. \(2021\)](#) to identify PNe candidates. This method comprises two steps: first, generating continuum-subtracted maps for each spectral channel within a specific wavelength range centred on the $[\text{O III}]\lambda 5007$ line; second, detecting PNe candidates by combining three wavelength-adjacent maps and selecting point sources that appear consistently across at least three of them. Despite the small area covered by the data, they were able to identify 34 PNe and estimate a distance modulus of $28.66^{+0.12}_{-0.28}$ mag ($5.4^{+0.3}_{-0.6}$ Mpc). This is one magnitude (~ 2 Mpc) larger than the typically accepted value. They note that the archival MUSE pointings cover a suboptimal region for PNLF studies, the galaxy’s centre, where gas and dust structures complicate PNe identification and hinder precise photometry, likely leading to an overestimated distance. Nevertheless, we proceed with the comparison since it could still provide an important validation of our results.

We have included the same MUSE archival data in our mosaic, so all PNe identified by [Jacoby et al. \(2024\)](#) are included in

our footprint. We identify in our catalogue only 21 of their 34 objects, and all of them are classified as PNe, except one (which we consider a SNR). Visual inspection suggests that most of the remaining 13 sources are either extremely faint in our $[\text{O III}]\lambda 5007$ map or appear as knots within the outflow-related $[\text{O III}]\lambda 5007$ emission. One exception is a source at the edge of the southern pointing, excluded from our catalogue because it appears as a pair of close candidates, making reliable photometry unfeasible. The orange points in Fig. 9 illustrate the photometric comparison between the two works. The scatter (0.17 mag) and offset (0.07 mag) are similar to those found in the comparison with [Rekola et al. \(2005\)](#), though the residuals reveal some structured trend, hinting at possible systematic differences.

[Jacoby et al. \(2024\)](#) used for their analysis the reduced version of the data publicly available through the ESO archive, which uses a different approach to the sky subtraction and exposure alignment. To assess whether this affects the measurements, we repeated our analysis using these publicly available cubes and found no significant difference for the brightest sources (Fig. 9, light blue triangles).

Following the same approach used for [Rekola et al. \(2005\)](#), we attempted to reproduce the [Jacoby et al. \(2024\)](#) PNLF using only the sources common to both catalogues⁶. Using all the sources we have in common, we obtain a distance of $28.47^{+0.14}_{-0.31}$ mag ($4.95^{+0.32}_{-0.70}$ Mpc). If we remove the two sources that were not used by [Jacoby et al. \(2024\)](#) in their fit, the result changes to $28.44^{+0.15}_{-0.32}$ mag ($4.88^{+0.34}_{-0.71}$ Mpc).

Our photometry yields generally fainter magnitudes than those in [Jacoby et al. \(2024\)](#), leading to a slightly smaller distance estimate. However, the errors are quite large, so the result is still within 1σ of their measurement. Moreover, this distance is significantly larger than what we obtain using our full PNe sample, supporting the interpretation by [Jacoby et al. \(2024\)](#) that the brightest PNe in the galaxy centre are likely missing.

⁶ Here we consider our original, best-estimate photometry.

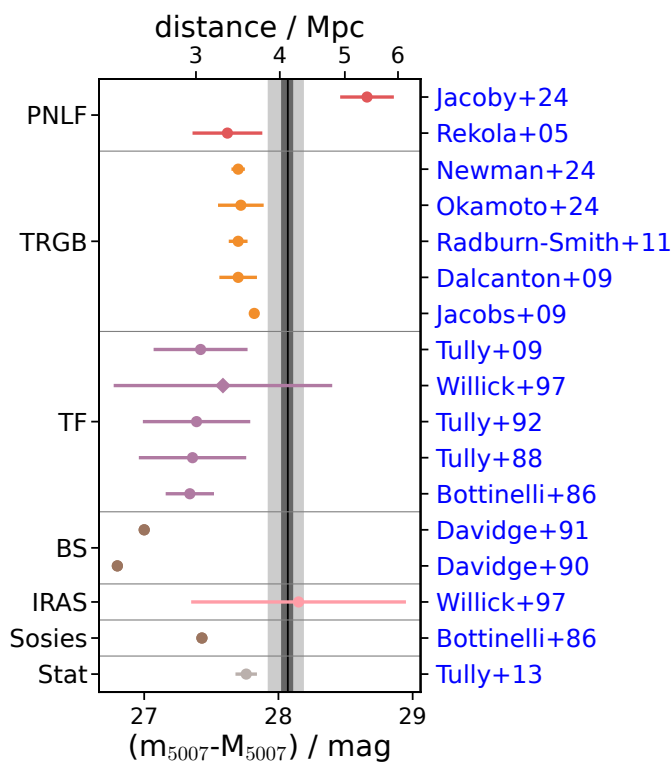


Fig. 8. Comparison between our measurement (solid black vertical line) with errors (1σ , dark colour, and 3σ , lighter colour) with distances from the literature. All measurements are divided depending on the method used. We use the following abbreviations: Planetary Nebula Luminosity Function (PNLF), Tip of the Red Giant Branch (TRGB), Tully-Fisher (TF), Brightest Stars (BS), Infra-Red Astronomical Satellite (IRAS), Sosies, and Statistical (Stat). Distances from: Bottinelli et al. (1986); Tully & Fisher (1988); Davidge & Pritchett (1990); Davidge et al. (1991); Tully et al. (1992); Willick et al. (1997); Rekola et al. (2005); Dalcanton et al. (2009); Jacobs et al. (2009); Tully et al. (2009); Radburn-Smith et al. (2011); Tully et al. (2013); Jacoby et al. (2024); Newman et al. (2024); Okamoto et al. (2024).

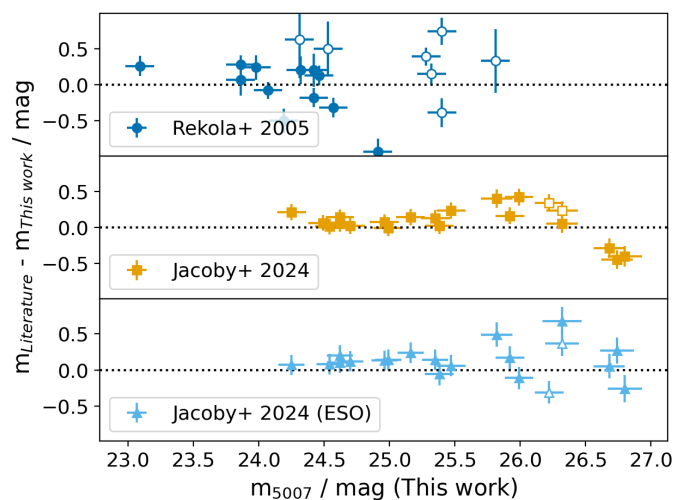


Fig. 9. Comparison between our PNe photometry, Rekola et al. (2005) and Jacoby et al. (2024). For Jacoby et al. (2024) we performed the comparison using both the data reduced by us, and the cubes directly recovered from the ESO archive. Solid symbols represent PNe that were used by the original authors in their PNLF computation. Open symbols represent objects that were not included in the final fit.

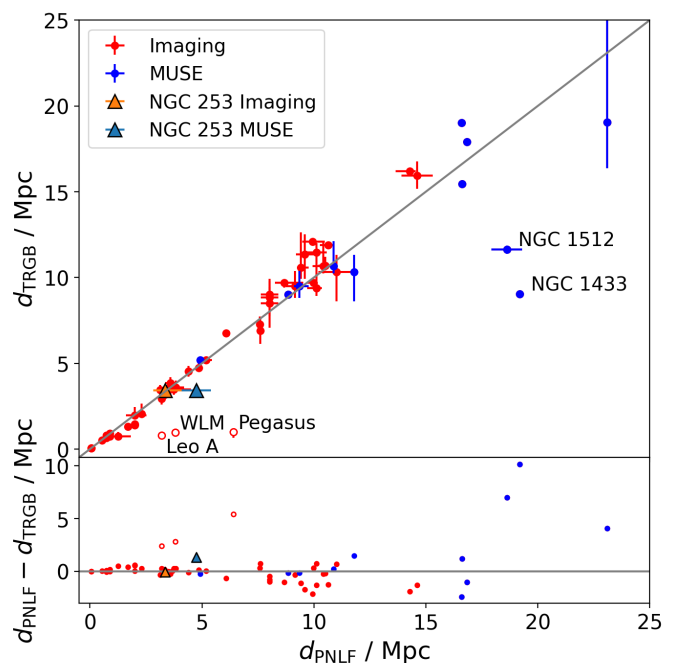


Fig. 10. Distance comparison for galaxies with both PNLF and TRGB measurements from NED⁷. Red points indicate galaxies where the PNLF was measured using imaging techniques, while blue points indicate PNLF measurements obtained with MUSE data. The grey line shows the one-to-one relation. The orange and light blue triangles identify the position of NGC 253 in the diagram when considering only imaging PNLF or MUSE-based PNLF respectively. Error bars represent the range between the minimum and maximum values obtained via a specific method. We also annotated in the main panel the position of a few notable sources, and we plot Pegasus, Leo A, and WLM with open red circles.

This exercise demonstrates two things. First, it shows that, even though our photometry shows some difference with respect to other measurements available in the literature, this does not significantly influence the distances recovered by the PNLF when limiting our analysis to the sample in common with previous works, and that therefore our result is reliable. Secondly, it shows that the Rekola et al. (2005) estimate of the distance of the galaxy, the only one in agreement with the commonly accepted TRGB-based value, is driven by the misclassification of one object. Therefore, all PNLF-based measurements of the distance to this galaxy are significantly overestimated compared to the TRGB-based distances. In the next section, we will investigate the possible origin of this tension.

5. Discussion

As we introduced in Sec. 4, the distance modulus we obtain from our analysis is 0.35 mag (0.6 Mpc) larger than what is recovered by other methods (mostly TRGB, ~ 27.72 mag, ~ 3.5 Mpc, Jacobs et al. 2009; Dalcanton et al. 2009; Radburn-Smith et al. 2011; Okamoto et al. 2024; Newman et al. 2024). Given the good reported agreement between these two methods in past work (e.g. Roth et al. 2021; Scheuermann et al. 2022; Jacoby et al. 2024), this discrepancy was unexpected. Figure 10 shows a direct comparison between TRGB and PNLF distances recovered from the NASA Extragalactic Database (NED) Redshift-Independent Distances database⁷. Since the database was last

⁷ <https://ned.ipac.caltech.edu/Library/Distances/>

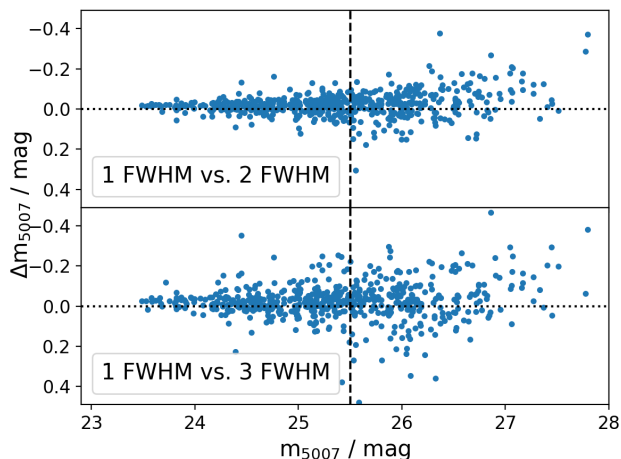


Fig. 11. Effect of the aperture correction on the measured magnitude of the PNe in our sample. Only the objects brighter than 25.5 mag (vertical dashed line) have been used for the PNLF fit. We define $\Delta[\text{OIII}]\lambda 5007$ as $m(X \times \text{FWHM}) - m(\text{FWHM})$ with X being either 2 or 3.

updated in 2020, it does not include more recent MUSE-based PNLF measurements. We therefore supplement the plot with additional distances published in Anand et al. (2021), Roth et al. (2021), Scheuermann et al. (2022), Jacoby et al. (2024), and Anand et al. (2024). The figure illustrates that TRGB- and PNLF-based distances follow a tight relation out to ~ 15 Mpc.⁸ Therefore, we are not considering these three points in the analysis. Beyond 15 Mpc, only a handful of MUSE-based PNLF measurements are available, with increased scatter driven primarily by NGC 1433 and NGC 1512. As discussed by Scheuermann et al. (2022) and Jacoby et al. (2024), these deviations are linked to the misidentification of the TRGB in their colour-magnitude diagrams (CMD).

In contrast, this explanation does not hold for NGC 253. Its distance is significantly lower, making it easier to identify the position of the TRGB in the CMD. In fact, its TRGB-based distance has been independently measured multiple times in the literature (Jacobs et al. 2009; Dalcanton et al. 2009; Radburn-Smith et al. 2011; Okamoto et al. 2024; Newman et al. 2024), and all estimates are in mutual agreement. On the other hand, the PNLF is not an easy method to apply to star-forming galaxies, where most of the $[\text{O III}]\lambda 5007$ emission is produced by other types of nebulae. Additionally, there are known cases where the PNLF yields inconsistent distances depending on the region of the galaxy sampled (Herrmann et al. 2008; Bhattacharya et al. 2021). Several observational effects, such as extinction, background subtraction, and aperture correction, can impact the photometry of PNe and hence the distance derived from the PNLF. In the following section, we examine these factors in more detail to investigate the origin of the discrepancy.

5.1. Aperture correction

The aperture correction is one of the most critical aspects of our analysis. It is essential to recover the full flux of a point-like

⁸ The three points that significantly deviate from the relation at low distances represent very nearby dwarf galaxies: Pegasus, Leo A and WLM. Their PNLF-based distances are early attempts and are based on a very limited sample of PNe (one for Pegasus, one for Leo A and two for WLM; Jacoby & Lesser 1981).

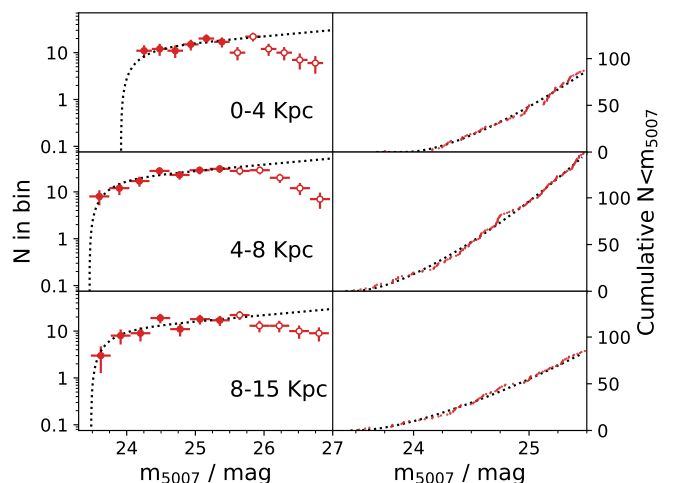


Fig. 12. PNLF for the three subsample of PNe at different galactocentric distances. The left column show the PNLF and their fit, while the right column show the cumulative luminosity function. Colours and symbols are the same as described in Fig. 6.

source when a small aperture, which does not encompass the entirety of the PSF, is used to perform photometry. Good aperture corrections should provide the same total flux for the same object regardless of the aperture size.

To assess whether the aperture correction could account for the discrepancy in our distance estimate, we conducted a series of validation tests. First, we repeated the photometry using apertures with diameters 2 and 3 times larger than the originals, and applying the corresponding aperture corrections. We then compared the resulting fluxes to our original measurements. We evaluated that doubling the diameter results in fluxes that are, on average, only 2% higher, with a standard deviation of 6%. Instead, tripling the diameter produces fluxes that are 3% higher on average, but with a slightly larger standard deviation (12%). The small average differences indicate that the aperture correction performs well overall, although the increased scatter suggests some object-to-object variability. However, Fig. 11 shows that the scatter is negligible for the brightest objects, which means that the effect of the aperture correction on the distance estimate is also negligible.

To confirm this, we used the new photometry to recompute the galaxy's distance. We obtain a distance modulus of $28.05^{+0.04}_{-0.05}$ mag ($4.07^{+0.07}_{-0.09}$ Mpc) when using the $2\times\text{FWHM}$ apertures and $28.02^{+0.04}_{-0.05}$ mag ($4.01^{+0.07}_{-0.09}$ Mpc) when using the $3\times\text{FWHM}$ apertures. The final result is, in both cases, within 1σ of our original measurement ($28.07^{+0.03}_{-0.05}$ mag or $4.10^{+0.07}_{-0.09}$ Mpc). We therefore conclude that, although our aperture correction method introduces some scatter, its effect on the final distance modulus is minimal and limited to at most 0.05 mag.

5.2. Radial variation of the PNLF

The PNLF has generally been found to be stable when selecting subsamples of PNe located in different regions of a galaxy (e.g. Hui et al. 1993; Ciardullo et al. 2004; Ciardullo 2013). However, some exceptions have been observed, both in the halo (e.g., M31; Bhattacharya et al. 2021) and within galaxy disks (e.g., Herrmann et al. 2008). The comparison we performed in Sect. 4.2 suggests that a radial dependence of the PNLF may also be present in NGC 253, as the distance recovered from PNe

Table 3. Summary of the three distance based samples and results of the fit.

Sample	All	Used	μ (mag)	D (Mpc)
All	571	320	$28.07^{+0.04}_{-0.05}$	$4.10^{+0.07}_{-0.09}$
0–4 kpc	158	87	$28.46^{+0.06}_{-0.09}$	$4.91^{+0.14}_{-0.21}$
4–8 kpc	251	148	$28.00^{+0.05}_{-0.08}$	$3.97^{+0.09}_{-0.14}$
> 8 kpc	162	85	$28.02^{+0.07}_{-0.10}$	$4.02^{+0.12}_{-0.19}$

Notes. The columns show: the name of the sample, the number of PNe contained in the sample, the number of PNe used in the PNLf fit, the distance modulus, the distance in Mpc.

Table 4. Results of the K-sample Anderson-Darling test applied to each couple of sub-samples.

Sample	Statistic	p-value	Significance
0–4 kpc vs 4–8 kpc	3.670	0.011	1%
0–4 kpc vs > 8 kpc	2.363	0.035	3%
4–8 kpc vs > 8 kpc	-1.122	0.250	25%

located in the central regions is significantly larger than that obtained using the full population.

To further explore a potential environmental dependence, we divided our PNe into subsamples based on their deprojected distance from the galaxy centre. We deproject the position of each object using the parameters listed in Table 1, which are adopted from the HyperLEDA catalogue (Makarov et al. 2014) and McCormick et al. (2013), and a standard distance of 3.5 Mpc (e.g., Okamoto et al. 2024). We then defined three subsamples: the first includes PNe located within the central 4 kpc of the galaxy; the second contains those between 4 kpc and 8 kpc; and the third includes all objects beyond 8 kpc. These boundaries were chosen to divide the galaxy’s semi-major axis into roughly equal parts while ensuring that each bin contains a sufficient number of PNe brighter than 25.5 mag (~ 100) to allow a reliable fit of the PNLf (see Table 3).

The result of the analysis is reported in Fig. 12. The plot shows that the central PNLf is almost 0.75 mag fainter than that obtained from the other two samples. As a consequence, the distance is significantly larger ($28.46^{+0.06}_{-0.09}$ mag, or $4.91^{+0.14}_{-0.21}$ Mpc), and it agrees with the value we derived in Sect. 4.2. The other two PNLfs appear mutually consistent, although the 4–8 kpc sample contains a larger number of sources. Indeed, the distance moduli we recover are $28.00^{+0.05}_{-0.08}$ mag ($3.97^{+0.09}_{-0.14}$ Mpc) and $28.02^{+0.07}_{-0.10}$ mag ($4.02^{+0.12}_{-0.19}$ Mpc) for the 4–8 kpc and >8 kpc samples respectively.

We performed a k-sample Anderson-Darling test for each pair of subsamples. The results are reported in Tab. 4, and they confirm that the central subsample is statistically inconsistent with being drawn from the same parent distribution as the other two subsamples at high significance levels (1% and 3%, respectively), while the two outer subsamples are fully consistent with being drawn from the same distribution.

Comparing the distances obtained from these subsamples with the measurement we performed using the full sample shows that excluding the central PNe changes the final measurement only marginally. This is somewhat expected, since the distance measurement is mostly driven by the brightest nebulae and, as

is clear from Fig. 12, they are not located in the centre of the galaxy.

The causes of the spatial variation of the PNLf could be several. If we exclude calibration issues, which are unlikely given the comparison performed in Sec. ??, other possibilities could be internal extinction due to dust or variations in the gas-phase metallicity, with the first being the most likely explanation. These properties could also affect the discrepancy between the PNLf and TRGB distances, so we will analyse them in the following sections.

5.3. Metallicity

As introduced in Sec. 4, empirical studies suggest that the zero point of the PNLf depends on the metallicity of the gas (e.g., Dopita et al. 1992; Ciardullo et al. 2002; Scheuermann et al. 2022), and, in particular, it increases when the metallicity decreases. Given the shallow relation and the metallicity of NGC 253, very close to solar ($12 + \log(\text{O}/\text{H}) = 8.69$ Beck et al. 2022), in Sec. 4 we ignored this effect, but here we will revise this assumption, considering also potential effects from the radial metallicity gradient of the galaxy.

Considering a solar metallicity from Asplund et al. (2009), the change in zero-point vs metallicity is described by the following relation (Ciardullo et al. 2002; Scheuermann et al. 2022):

$$\Delta M_{5007}^* = 0.928[\text{O}/\text{H}]^2 - 0.109[\text{O}/\text{H}] + 0.004. \quad (5)$$

We can invert this equation to return the expected metallicity of the gas given the ΔM_{5007}^* needed to obtain a distance of 3.5 Mpc from our PNLf. We consider only the lower solution of the equation, given that the relation between ΔM_{5007}^* and metallicity has been characterised for metallicities lower than solar. Obtaining a distance of 3.5 Mpc from our PNe sample would require $M_{5007}^* = -4.23$ mag, which corresponds to $\Delta M_{5007}^* = 0.31$ and a metallicity of $12 + \log(\text{O}/\text{H}) = 8.17$ ($\sim 1/3 Z_{\odot}$). From the analysis of ~ 1000 H II regions identified by McClain et al. (in prep) we recover a preliminary gradient of -0.28 dex/ R_{25} (Congiu et al., in prep.), which makes it impossible to reach an average metallicity of $12 + \log(\text{O}/\text{H}) = 8.17$ starting from the Beck et al. (2022) nuclear value. This gradient also rules out metallicity as the origin of the fainter PNLf observed in the central part of the galaxy, as it would require a heavily inverted gradient, which is clearly not observed.

5.4. Extinction

When studying the PNLf of a galaxy, extinction is a delicate matter. First, the foreground extinction caused by the Milky Way and the extinction caused by dust present in the host galaxy should be removed from the $[\text{O III}]\lambda 5007$ fluxes. Such dust causes the PNe to appear fainter than they are, and in the most extreme cases it can also prevent the detection of bright objects located inside or behind the screen. Second, intrinsic extinction, that is, the extinction caused by dust produced by the AGB star during the final stages of its evolution and located within the PN itself, has traditionally not been removed (Ciardullo & Jacoby 1999; García-Rojas et al. 2018; Davis et al. 2018). As a result, the empirical functional form of the PNLf implicitly contains this bias, and any attempt to correct for intrinsic extinction may require a redetermination of the empirical functional form itself.

Removing the foreground Milky Way extinction is straightforward, as we describe in Sec. 3.3. However, correcting the internal extinction without removing the PNe intrinsic extinction

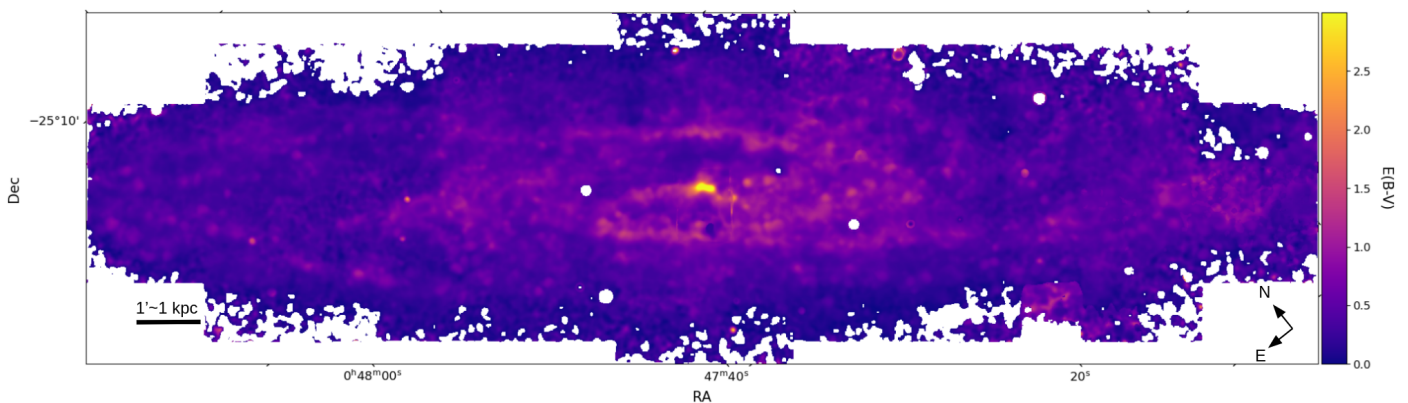


Fig. 13. $E(B - V)$ map of NGC 253. The $E(B - V)$ has been calculated from the Balmer decrement using a convolved (to a 5 arcsec FWHM Gaussian PSF) and binned version of the data, in order to detect both $H\alpha$ and $H\beta$ across the majority of the FOV.

is extremely challenging. A standard approach such as estimating the $E(B - V)$ of each nebula through the Balmer decrement of their spectrum is not an option, since it does not differentiate between the host galaxy extinction and the intrinsic PN extinction. In addition, simple arguments based on the vertical distribution of PNe and dust in galaxies suggest that, in most cases, the host extinction should not affect the PNLF (e.g., [Feldmeier et al. 1997](#)). Under typical conditions, there should be a large enough number of bright and unextinguished PNe to not affect the distance estimate, so only the foreground Galactic extinction is typically applied to the data. However, NGC 253 is a highly inclined galaxy with prominent dust features clearly visible throughout the disk, so extinction could play a more significant role.

5.4.1. Extinction Map

In [Fig. 13](#) we show the $E(B - V)$ map of NGC 253 recovered from the Balmer decrement. To obtain it, we convolved our mosaic to an angular resolution of 5 arcsec⁹ and binned it to 0.8 arcsec px^{-1} , to ensure detection of $H\alpha$ and $H\beta$ across most of the FOV. We then estimated the $E(B - V)$ assuming a theoretical $H\alpha/H\beta = 2.86$ (Case B recombination [Osterbrock & Ferland 2006](#)), a [Cardelli et al. \(1989\)](#) extinction law and $R_V = 3.1$. The resulting map shows a median $E(B - V)$ of ~ 0.36 mag ($A(V) \sim 1.1$ mag), with peaks of >6 mag ($A(V) > 18$ mag) close to the centre of NGC 253. [Rekola et al. \(2005\)](#) determined that for an extinction similar to our average one, the effect on the measured distance modulus should be of the order of a few 0.1 mag¹⁰. The discrepancy between our distance modulus and that recovered by TRGB measurements from, for example, [Okamoto et al. \(2024\)](#), is ~ 0.35 mag, which is, indeed, in line with the prediction of [Rekola et al. \(2005\)](#).

The MUSE extinction map represents the extinction produced by the dust screen in front of the $H\alpha$ and $H\beta$ emitting gas. In the case of a dusty interstellar medium with embedded emission, this represents approximately half of the total possible extinction. We do not know the position of each PN along the line of sight, and we also know that PNe and dust typically follow different distributions, especially in the vertical direction,

⁹ We assumed an average PSF FWHM of 0.8 across the mosaic (see [Sec. 3.2](#)) and we convolved it using a 2D Gaussian Kernel with the FWHM needed to recover a final FWHM of 5 arcsec. The spatial and spectral variation of the final FWHM is of the order of 0.1 arcsec

¹⁰ [Rekola et al. \(2005\)](#) do not provide a model that we could test. Our analysis is based mainly on the discussion in their [Sec. 3](#) and [Fig. 4](#)

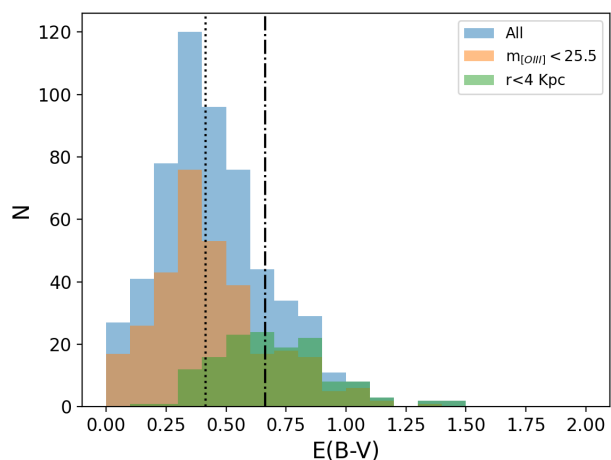


Fig. 14. Maximum host galaxy $E(B - V)$ associated with each PN. In blue we show the full sample, in orange only the PNe brighter than 25.5 mag, and in green the PNe located within 4 kpc from the centre of the galaxy. The dotted line represents the median $E(B - V)$ for the full sample, while the dashed-dotted line shows the median for PNe in the centre of the galaxy.

so we cannot use this map to directly correct the fluxes of our PNe. Nevertheless, comparing the extinction map with the position of our PNe can still help us gauge its effect on the PNLF. For each PN, we used the 5 arcsec resolution extinction map shown in [Fig. 13](#) to recover the average $E(B - V)$ contained in the same aperture that we used to correct the $[\text{O III}]\lambda 5007$ fluxes for background emission. We do not simply measure the extinction at the exact location of our PNe to avoid including any effect of the intrinsic extinction, although this is probably not necessary given the resolution of our convolved data. [Figure 14](#) shows the distribution of $E(B - V)$ associated with the PNe in the sample (blue histogram). We have a distribution ranging from $E(B - V) = 0$ to $E(B - V) = 1.44$ mag ($A(V) \sim 4.45$ mag) with an average of 0.45 mag and a median of 0.41 mag ($A(V) \sim 1.40$ mag and 1.27 mag, respectively). This confirms that we are in a regime in which the effects of extinction on the PNLF are no longer negligible. If we consider only the PNe brighter than 25.5 mag (those included in the fit, orange histogram), we see that they have a very similar distribution. Finally, in green, we show the $E(B - V)$ distribution for PNe located within 4 kpc of the nucleus of the galaxy. As expected, this sample includes the objects in the

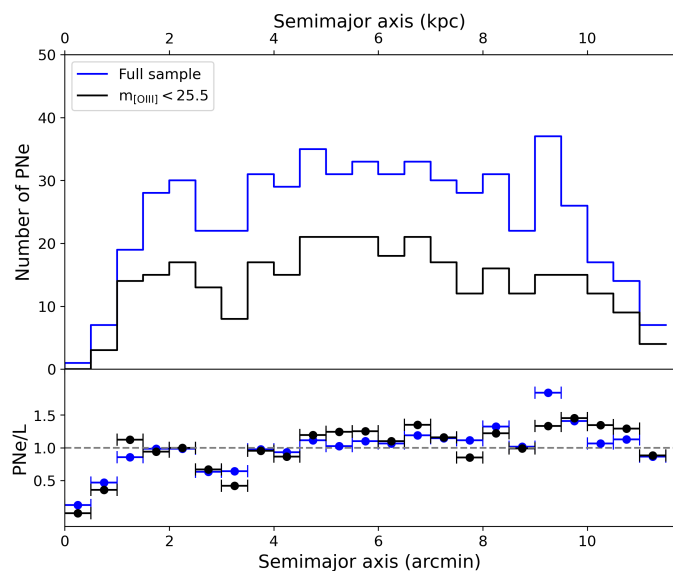


Fig. 15. Distribution of PNe as a function of distance from the centre of the galaxy. The top panel shows the number of PNe contained in concentric elliptical rings with growing semimajor axis. The bottom panel shows the luminosity-specific PNe number density measured in the same rings and normalized of its average value, since we are interested in the trend and not on its absolute value. We show the full sample in blue and the sample with $m_{\text{[OIII]}} < 25.5$ mag in black.

high-extinction tail of the distribution, which could explain the significant difference between the distance estimate we obtain using only this sub-sample of sources (see Sec. 5.2).

5.4.2. Completeness

Another way the extinction could impact the PNLF is by affecting the completeness of the PNe sample, particularly in the dusty galaxy centre. Figure 15 shows how the number of PNe in concentric elliptical annuli changes as a function of distance from the centre of the galaxy both as an absolute measurement (top panel) and as the ratio between the number of PNe and the flux contained in the ellipse (bottom panel). To measure these quantities, we defined a series of ellipses centred on the centre of the galaxy and with constant PA and ellipticity and we counted how many PNe fell in each elliptical ring. We then used the WFI R-band image presented in Sec. 2.1.1 to extract the integrated flux in the same areas, masking bright stars, and we computed the the ratio between the number of PNe and the flux contained in each annulus¹¹. This quantity has been shown to be quite independent from the properties of the stellar population of a galaxy (Ciardullo et al. 1989; Buzzoni et al. 2006), therefore any variations could indicate changes in the PNe sample completeness, perhaps due to dust extinction. Figure 15 shows that this quantity is relatively stable across the disk. Only rings with more that 50% coverage in our mosaic are included in the plot. At distances < 4 kpc however, we see we see a significant change in PNe/L, indicating a drop in completeness. This happens both at the very centre, where we have the starburst ring and higher measured values of $E(B - V)$, and around ~ 3.5 kpc from the centre, which correspond approximately to the end of the bar. Here, both Fig. 1 and Fig. 13 show strong dust lanes and high extinction values.

¹¹ Since we are interested in the relative distribution of these points, and not in their absolute value, we did not convert the fluxes in luminosities.

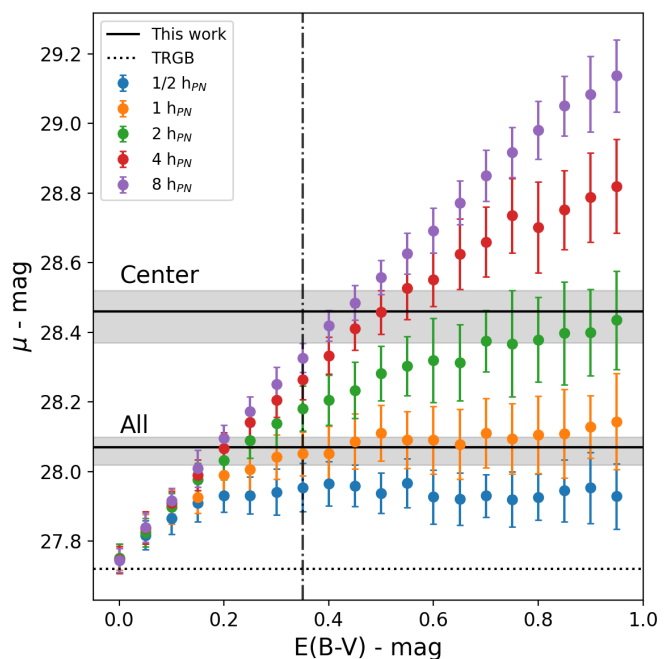


Fig. 16. Effects of the extinction on the distance modulus measured via the PNLF. The points show how the distance modulus estimated via a sample of PNe extracted from a PNLF with fixed zero-point and distance modulus ($M^* = -4.54$ mag and 27.72 mag respectively) changes when applying an increasing amount of extinction. In this model, both PNe and extinction (dust) follow a Laplace distribution, as described in Sec. 5.4. Different colours represent different ratios between the PNe and dust scale height. The solid horizontal lines represent our measurement of the distance modulus of the galaxy when considering both the full sample (bottom line) and only the PNe close to the centre of the galaxy (top line), while the grey areas represent their uncertainties. The dashed horizontal line represent a distance modulus of 27.72 mag, the expected one from the TRGB-based distances from the literature. Finally, the vertical dot-dashed line represents the average $E(B - V)$ we measured from the extinction map shown in Fig. 13.

5.4.3. Modelling the effects of extinction on the PNLF

In order to quantitatively assess the impact of dust extinction on the PNLF, we employ a straightforward model that describes the vertical distribution of dust and PNe within a disk to determine whether we could obtain a distance of 4.10 Mpc by applying extinction to samples of PNe extracted from the expected PNLF of a galaxy situated 3.5 Mpc away (27.72 mag), as is the case of NGC 253. Following the assumptions of Rekola et al. (2005), we consider that both PNe and dust are distributed following a Laplace distribution (also known as a double exponential distribution). This represents their vertical distribution across the galactic disk, where the maximum of the probability coincides with the disk plane. To keep the model simple, we assume a face-on disk, ignoring potential inclination effects. We first extract a sample of PNe from the PNLF and assign them a location within the disk by extracting it from their Laplace distribution. We then recover the expected extinction at their location from the cumulative distribution of dust normalised to the maximum extinction we considered. The extinction is then applied assuming a Cardelli et al. (1989) extinction law, and an $R_V = 3.1$. Finally, the modified PNLF was fitted with the method from Sec. 4.

We varied the maximum extinction from 0 to $E(B - V) = 1$ mag. Then, we set a fixed scale height for the PNe and examined multiple scale heights for the dust: half, one, two,

four, and eight times the PNe scale height. For each combination of parameters, we repeated the entire process 50 times, considering the mean distance as our measurement and its standard deviation as our error. The results of this analysis are presented in Fig. 16. As expected, the extinction influences the distance inferred from the PNLF. Larger maximum extinctions result in more pronounced effects, making the galaxy appear further away, until a plateau is reached. Beyond this plateau, further increases in extinction do not affect the distance. The $E(B - V)$ at which the plateau emerges depends on the relative scale heights of dust and PNe. When both are similarly distributed or when the dust has a higher scale height, we can recover our findings based on the anticipated PNLF of NGC 253. The $E(B - V)$ at which this alignment occurs is approximately 0.3 mag if dust and PNe share the same scale height, consistent with [Rekola et al. \(2005\)](#). If the dust scale height exceeds that of the PNe, we need only and $E(B - V)$ of 0.2 mag to explain our discrepancy. Finally, if the PNe scale height is larger than the dust one, the plateau is reached at very low $E(B - V)$. In this case, the difference between the measured distance modulus and the expected one is small and cannot explain our discrepancy. This result is in line with the argument exposed by [Feldmeier et al. \(1997\)](#), which states that in this scenario there should always be a large enough number of bright and unextinguished PNe to not affect the final distance.

Extinction can also explain the difference between the distances recovered from disk and the central PNLFs. In this case, Fig. 16 suggests that both a larger amount of extinction and a larger dust scale height are needed to explain our observations. In particular, it shows that the dust needs to be distributed with a scale height that is at least twice as large as the PNe one, while the maximum extinction needs to be ≥ 0.4 , even though it changes significantly depending on the dust scale height.

This analysis suggests that internal extinction within the host galaxy is responsible for the discrepancies we observe, as well as for the differences in zero-point between the central and the disk PNLF. In particular, it suggests that in NGC 253 the dust is distributed with a similar scale height relative to the PNe in the disk, and a much larger scale height if we consider only the region close to the centre of the galaxy. This was not expected, since studies of both the Milky Way ([Allen 1973](#); [Li et al. 2018](#)) and other edge-on nearby galaxies (e.g. [Xilouris et al. 1999](#); [Bianchi 2007](#); [De Geyter et al. 2014](#)) show how they exhibit a thin disk of dust, with a scale height half that of the stellar disk (where the PNe reside). In NGC 253 the starburst-driven outflow might be ejecting large quantities of dust-rich material from the centre of the galaxy, boosting the dust scale height. This effect is stronger close to the outflow, which is why we need a much larger scale height to explain the distance recovered from the central PNLF. The dust then settles when it moves further away from the outflow, but into a thicker disk with respect to more quiescent galaxies.

The proximity of NGC 253 and availability of highly precise distance measurements from multiple techniques show how the assumption that the PNLF is independent of the amount of dust in a galaxy is not always correct. As stated by [Jacoby et al. \(2024\)](#), having large and heterogeneous galaxy samples with well-sampled PNLFs is essential to characterise the circumstances where the dust distribution significantly biases the PNLF distance. While correcting for the host galaxy dust extinction at any given position in the disk where a PN is found is challenging, our growing multi-wavelength views of the dust-rich ISM, along with the potential to develop rich kinematic models from the combined stellar and gas disk components, could be used to

develop a statistical 3D approach to forward-model the line-of-sight dust extinction of the PNe population. Such an analysis is beyond the scope of this work but may present a novel way to refine the use of the PNLF as a rung in the cosmological distance ladder.

6. Summary and Conclusions

This work presents a new MUSE mosaic of the nearby starburst galaxy NGC 253. The mosaic includes 103 MUSE pointings covering an approximate area of $20 \times 5 \text{ armin}^2$ with ~ 9 million spectra, and represents the largest mosaic of an extragalactic source ever observed by MUSE so far, not counting the sparse mosaic of the Large Magellanic Cloud ([Boyce et al. 2017](#)). The data were observed as part of two ESO programmes (108.2289 and 10102.B-0078(A)) for a total of ~ 53.5 hrs of observing time. Exposures were reduced using the official ESO MUSE pipeline ([Weilbacher et al. 2020](#)) through the `pymusepipe` wrapper ([Emsellem et al. 2022](#)) and processed with the PHANGS data analysis pipeline, following the procedures described in [Emsellem et al. \(2022\)](#). Special care has been given to the sky subtraction, given the low redshift of the galaxy.

We then exploit moment-zero maps of the main emission lines ($[\text{O III}]\lambda 5007$, $\text{H}\alpha$, and $[\text{S II}]\lambda\lambda 6717, 6731$) to identify a sample of 571 PNe. We use 320 of them (those brighter than 25.5 mag, our estimated completeness limit) to build the PNLF of the galaxy and recover its distance. Following the procedure described in [Scheuermann et al. \(2022\)](#), we estimate a distance modulus of $28.07^{+0.03}_{-0.05}$ mag ($4.10^{+0.07}_{-0.09}$ Mpc), which is ~ 0.35 mag (0.6 Mpc) larger than expected from previous independent distance estimates from PNLF fitting and the TRGB method. In particular, the TRGB-based distance (~ 27.72 mag, 3.5 Mpc) has been independently confirmed several times over the last 15 years, proving itself to be a reliable reference. The PNLF analysis revealed the following:

- The distance recovered by [Rekola et al. \(2005\)](#) ($27.62^{+0.16}_{-0.26}$ mag or $3.34^{+0.26}_{-0.38}$ Mpc) was driven by the misclassification of their brightest region, which now appears as an H II regions. Removing it from their sample, reconciles their distance with ours.
- The zero point of the relation changes significantly when considering only PNe located in the centre of the galaxy versus those located in the rest of the disk. In particular, the inner PNLF returns a distance that is ~ 0.45 mag (0.9 Mpc) larger than the distance recovered from the rest of the disk.
- We reject metallicity as the origin of the discrepancy that we observe between our measurement and the literature. Preliminary measurement of the gas phase metallicity and its gradient shows values corresponding to a negligible correction of the PNLF zero-point.
- We reject metallicity also as the origin of the spatial variation of the PNLF, since the observed behaviour would require an inverted metallicity gradient not observed in the galaxy.
- A Balmer-decrement-based extinction map shows that the galaxy is affected by a significant amount of extinction. We estimate a median $E(B - V)$ of ~ 0.36 mag ($A(V) \sim 1.1$ mag), with peaks of > 6 mag ($A(V) > 18$ mag) close to the NGC 253 centre.
- A simple model for the distribution of the PNe and dust shows that we can reproduce our results for the whole galaxy if we assume a maximum $E(B - V) \sim 0.3$ mag and the same scale height for dust and PNe. Reproducing the estimate from the central PNLF, requires the dust to be distributed

with at least twice the PNe scale height. This is in contrast with what is expected from scale height studies of the Milky Way and other nearby edge on galaxies (e.g. Allen 1973; Xilouris et al. 1999; Bianchi 2007; De Geyter et al. 2014), but it is compatible with a scenario where the starburst-driven outflow is enhancing the vertical distribution of dust in the NGC 253.

In conclusion, this work shows that the PNLF is not a reliable method to estimate the distance of NGC 253, because of its high dust content and its peculiar distribution. In general, it shows that dust should not be ignored in the PNLF analysis, especially when working on galaxies characterised by high inclination and dust content, and that we need more galaxies with a well sampled PNLF to better characterise these effects.

Data availability

Datacubes and DAP products are available in the CADIC (<https://www.canfar.net/storage/vault/list/phangs/RELEASES/PHANGS-MUSE-NGC253>) and ESO Phase 3 archive (TBD).

Acknowledgements. The authors would like to thank our referee, Dr. Micheal Richer, for the excellent comments that helped improve this work. Based on observations collected at the European Organisation for Astronomical Research in the Southern Hemisphere under ESO programmes 108.2289 (PI: Congiu) and 0102.B-0078(A) (PI: Zschaechner). This work was carried out as part of the PHANGS collaboration. FS and KK acknowledge support from the Deutsche Forschungsgemeinschaft (DFG, German Research Foundation) in the form of an Emmy Noether Research Group (grant number KR4598/2-1, PI Kreckel) and the European Research Council's starting grant ERC StG-101077573 ("ISM-METALS"). OE acknowledges funding from the Deutsche Forschungsgemeinschaft (DFG, German Research Foundation) – project-ID 541068876. E.C. and J.H. acknowledge the financial support from the visitor and mobility program of the Finnish Centre for Astronomy with ESO (FINCA). JEMD acknowledges support from project UNAM DGAPA-PAPIIT IG 101025, Mexico. A.D.B. and S.A.C. acknowledge support from the NSF under award AST-2108140. R.S.K. acknowledges financial support from the ERC via Synergy Grant "ECOGAL" (project ID 855130), from the German Excellence Strategy via the Heidelberg Cluster "STRUCTURES" (EXC 2181 - 390900948), and from the German Ministry for Economic Affairs and Climate Action in project "MAINN" (funding ID 50002206). RSK also thanks the 2024/25 Class of Radcliffe Fellows for highly interesting and stimulating discussions. This research has made use of the NASA/IPAC Extragalactic Database, which is funded by the National Aeronautics and Space Administration and operated by the California Institute of Technology. This research has made use of the Astrophysics Data System, funded by NASA under Cooperative Agreement 80NSSC21M00561. This research made use of Astropy, a community-developed core Python package for Astronomy (Astropy Collaboration et al. 2013, 2018), Matplotlib (Hunter 2007), MPDAF (Bacon et al. 2016; Piqueras et al. 2017), NumPy (Harris et al. 2020), Photutils (Bradley et al. 2024), Pyneb (Luridiana et al. 2015), SciPy (Virtanen et al. 2020), Scikit-learn (Pedregosa et al. 2011).

References

Acker, A., Marcout, J., Ochsenbein, F., et al. 1992, The Strasbourg-ESO Catalogue of Galactic Planetary Nebulae. Parts I, II. (Garching: European Southern Observatory)
 Allen, C. W. 1973, *Astrophysical quantities*
 Anand, G. S., Lee, J. C., Van Dyk, S. D., et al. 2021, *MNRAS*, 501, 3621
 Anand, G. S., Tully, R. B., Cohen, Y., et al. 2024, *ApJ*, 973, 83
 Arnaboldi, M., Aguerri, J. A. L., Napolitano, N. R., et al. 2002, *AJ*, 123, 760
 Asplund, M., Grevesse, N., Sauval, A. J., & Scott, P. 2009, *ARA&A*, 47, 481
 Astropy Collaboration, Price-Whelan, A. M., Sipőcz, B. M., et al. 2018, *AJ*, 156, 123
 Astropy Collaboration, Robitaille, T. P., Tollerud, E. J., et al. 2013, *A&A*, 558, A33
 Bacon, R., Piqueras, L., Conseil, S., Richard, J., & Shepherd, M. 2016, MPDAF: MUSE Python Data Analysis Framework, Astrophysics Source Code Library, record ascl:1611.003
 Bailin, J., Bell, E. F., Chappell, S. N., Radburn-Smith, D. J., & de Jong, R. S. 2011, *ApJ*, 736, 24

Bates, D. R. 1946, *MNRAS*, 106, 509
 Bauer, M., Pietsch, W., Trinchieri, G., et al. 2007, *A&A*, 467, 979
 Beck, A., Lebouteiller, V., Madden, S. C., et al. 2022, *A&A*, 665, A85
 Bendo, G. J., Beswick, R. J., D'Cruze, M. J., et al. 2015, *MNRAS*, 450, L80
 Bhattacharya, S., Arnaboldi, M., Gerhard, O., et al. 2021, *A&A*, 647, A130
 Bianchi, S. 2007, *A&A*, 471, 765
 Bolatto, A. D., Warren, S. R., Leroy, A. K., et al. 2013, *Nature*, 499, 450
 Bottinelli, L., Gougouenheim, L., Paturel, G., & Teerikorpi, P. 1986, *A&A*, 156, 157
 Boyce, H., Lützgendorf, N., van der Marel, R. P., et al. 2017, *ApJ*, 846, 14
 Bradley, L., Sipőcz, B., Robitaille, T., et al. 2024, *astropy/photutils: 1.11.0*
 Bundy, K., Bershady, M. A., Law, D. R., et al. 2015, *ApJ*, 798, 7
 Buzzoni, A., Arnaboldi, M., & Corradi, R. L. M. 2006, *MNRAS*, 368, 877
 Cappellari, M. 2017, *MNRAS*, 466, 798
 Cardelli, J. A., Clayton, G. C., & Mathis, J. S. 1989, *ApJ*, 345, 245
 Ciardullo, R. 2010, *PASA*, 27, 149
 Ciardullo, R. 2013, in *IAU Symposium*, Vol. 289, *Advancing the Physics of Cosmic Distances*, ed. R. de Grijs, 247–254
 Ciardullo, R., Durrell, P. R., Laychak, M. B., et al. 2004, *ApJ*, 614, 167
 Ciardullo, R., Feldmeier, J. J., Jacoby, G. H., et al. 2002, *ApJ*, 577, 31
 Ciardullo, R. & Jacoby, G. H. 1999, *ApJ*, 515, 191
 Ciardullo, R., Jacoby, G. H., Ford, H. C., & Neill, J. D. 1989, *ApJ*, 339, 53
 Cronin, S. A., Bolatto, A. D., Congiu, E., et al. 2025, *ApJ*, in press
 Croom, S. M., Lawrence, J. S., Bland-Hawthorn, J., et al. 2012, *MNRAS*, 421, 872
 Dalcanton, J. J., Williams, B. F., Seth, A. C., et al. 2009, *ApJS*, 183, 67
 Davidge, T. J., Le Fevre, O., & Clark, C. C. 1991, *ApJ*, 370, 559
 Davidge, T. J. & Pritchett, C. J. 1990, *AJ*, 100, 102
 Davis, B. D., Ciardullo, R., Jacoby, G. H., Feldmeier, J. J., & Indahl, B. L. 2018, *ApJ*, 863, 189
 De Geyter, G., Baes, M., Camps, P., et al. 2014, *MNRAS*, 441, 869
 Della Bruna, L., Adamo, A., Amram, P., et al. 2022, *A&A*, 660, A77
 Della Bruna, L., Adamo, A., Bik, A., et al. 2020, *A&A*, 635, A134
 D'Odorico, S., Dopita, M. A., & Benvenuti, P. 1980, *A&AS*, 40, 67
 Dopita, M. A., Jacoby, G. H., & Vassiliadis, E. 1992, *ApJ*, 389, 27
 Draine, B. T. 2011, *Physics of the Interstellar and Intergalactic Medium*
 Drory, N., Blanc, G. A., Kreckel, K., et al. 2024, *AJ*, 168, 198
 Emsellem, E., Schinnerer, E., Santoro, F., et al. 2022, *A&A*, 659, A191
 Erroz-Ferrer, S., Carollo, C. M., den Brok, M., et al. 2019, *MNRAS*, 484, 5009
 Feldmeier, J. J., Ciardullo, R., & Jacoby, G. H. 1997, *ApJ*, 479, 231
 Fitzpatrick, E. L. 1999, *PASP*, 111, 63
 Gaia Collaboration, Brown, A. G. A., Vallenari, A., et al. 2018, *A&A*, 616, A1
 García-Rojas, J., Delgado-Inglada, G., García-Hernández, D. A., et al. 2018, *MNRAS*, 473, 4476
 Grasha, K., Chen, Q. H., Battisti, A. J., et al. 2022, *ApJ*, 929, 118
 Hanuschik, R. W. 2003, *A&A*, 407, 1157
 Harris, C. R., Millman, K. J., van der Walt, S. J., et al. 2020, *Nature*, 585, 357
 Hartke, J., Arnaboldi, M., Gerhard, O., et al. 2020, *A&A*, 642, A46
 Hartke, J., Arnaboldi, M., Longobardi, A., et al. 2017, *A&A*, 603, A104
 Herrmann, K. A., Ciardullo, R., Feldmeier, J. J., & Vinciguerra, M. 2008, *ApJ*, 683, 630
 Hlavacek-Larrondo, J., Carignan, C., Daigle, O., et al. 2011, *MNRAS*, 411, 71
 Hui, X., Ford, H. C., Ciardullo, R., & Jacoby, G. H. 1993, *ApJ*, 414, 463
 Hunter, J. D. 2007, *Computing in Science & Engineering*, 9, 90
 Husemann, B., Jahnke, K., Sánchez, S. F., et al. 2013, *A&A*, 549, A87
 Iodice, E., Arnaboldi, M., Rejkuba, M., et al. 2014, *A&A*, 567, A86
 Jacobs, B. A., Rizzi, L., Tully, R. B., et al. 2009, *AJ*, 138, 332
 Jacoby, G. H. 1989, *ApJ*, 339, 39
 Jacoby, G. H., Ciardullo, R., Roth, M. M., Arnaboldi, M., & Weillbacher, P. M. 2024, *ApJS*, 271, 40
 Jacoby, G. H. & De Marco, O. 2002, *AJ*, 123, 269
 Jacoby, G. H. & Lesser, M. P. 1981, *AJ*, 86, 185
 Jarrett, T. H., Cluver, M. E., Brown, M. J. I., et al. 2019, *ApJS*, 245, 25
 Kippenhahn, R., Weigert, A., & Weiss, A. 2013, *Stellar Structure and Evolution*
 Kopsacheili, M., Zezas, A., & Leonidaki, I. 2020, *MNRAS*, 491, 889
 Krieger, N., Bolatto, A. D., Walter, F., et al. 2019, *ApJ*, 881, 43
 Leroy, A. K., Bolatto, A. D., Ostriker, E. C., et al. 2015, *ApJ*, 801, 25
 Leroy, A. K., Sandstrom, K. M., Lang, D., et al. 2019, *ApJS*, 244, 24
 Leroy, A. K., Schinnerer, E., Hughes, A., et al. 2021, *ApJS*, 257, 43
 Li, J., Kreckel, K., Sarbadhicary, S., et al. 2024, *A&A*, 690, A161
 Li, L., Shen, S., Hou, J., et al. 2018, *ApJ*, 858, 75
 Lindegren, L., Hernández, J., Bombrun, A., et al. 2018, *A&A*, 616, A2
 Longobardi, A., Arnaboldi, M., Gerhard, O., et al. 2013, *A&A*, 558, A42
 Lopez, S., Lopez, L. A., Nguyen, D. D., et al. 2023, *ApJ*, 942, 108
 Lucero, D. M., Carignan, C., Elson, E. C., et al. 2015, *MNRAS*, 450, 3935
 Luridiana, V., Morisset, C., & Shaw, R. A. 2015, *A&A*, 573, A42
 Makarov, D., Prugniel, P., Terekhova, N., Courtois, H., & Vauglin, I. 2014, *A&A*, 570, A13
 McCormick, A., Veilleux, S., & Rupke, D. S. N. 2013, *ApJ*, 774, 126
 McLeod, A. F., Ali, A. A., Chevance, M., et al. 2021, *MNRAS*, 508, 5425

- Moffat, A. F. J. 1969, *A&A*, 3, 455
- Newman, M. J. B., McQuinn, K. B. W., Skillman, E. D., et al. 2024, *ApJ*, 966, 175
- Nossal, S. M., Mierkiewicz, E. J., Roesler, F. L., et al. 2019, *Journal of Geophysical Research (Space Physics)*, 124, 10,674
- Okamoto, S., Ferguson, A. M. N., Arimoto, N., et al. 2024, *ApJ*, 967, L24
- Osterbrock, D. E. & Ferland, G. J. 2006, *Astrophysics of gaseous nebulae and active galactic nuclei* (University Science Books)
- Pedregosa, F., Varoquaux, G., Gramfort, A., et al. 2011, *Journal of Machine Learning Research*, 12, 2825
- Piqueras, L., Conseil, S., Shepherd, M., et al. 2017, *arXiv e-prints*, arXiv:1710.03554
- Radburn-Smith, D. J., de Jong, R. S., Seth, A. C., et al. 2011, *ApJS*, 195, 18
- Reid, W. A. & Parker, Q. A. 2010, *MNRAS*, 405, 1349
- Rekola, R., Richer, M. G., McCall, M. L., et al. 2005, *MNRAS*, 361, 330
- Rodríguez-González, A., Hernández-Martínez, L., Esquivel, A., et al. 2015, *A&A*, 575, A1
- Roth, M. M., Jacoby, G. H., Ciardullo, R., et al. 2021, *ApJ*, 916, 21
- Rousseau-Nepton, L., Martin, R. P., Robert, C., et al. 2019, *MNRAS*, 489, 5530
- Rousseau-Nepton, L., Robert, C., Martin, R. P., Drissen, L., & Martin, T. 2018, *MNRAS*, 477, 4152
- Sánchez, S. F., Kennicutt, R. C., Gil de Paz, A., et al. 2012, *A&A*, 538, A8
- Scheuermann, F., Kreckel, K., Anand, G. S., et al. 2022, *MNRAS*, 511, 6087
- Schlafly, E. F. & Finkbeiner, D. P. 2011, *ApJ*, 737, 103
- Schönberner, D., Jacob, R., Sandin, C., & Steffen, M. 2010, *A&A*, 523, A86
- Solomon, S. C., Hays, P. B., & Abreu, V. J. 1988, *J. Geophys. Res.*, 93, 9867
- Stetson, P. B. 1987, *PASP*, 99, 191
- Strickland, D. K., Heckman, T. M., Weaver, K. A., & Dahlem, M. 2000, *AJ*, 120, 2965
- Tully, R. B., Courtois, H. M., Dolphin, A. E., et al. 2013, *AJ*, 146, 86
- Tully, R. B. & Fisher, J. R. 1977, *A&A*, 54, 661
- Tully, R. B. & Fisher, J. R. 1988, *Catalog of Nearby Galaxies* (Cambridge University Press)
- Tully, R. B., Rizzi, L., Shaya, E. J., et al. 2009, *AJ*, 138, 323
- Tully, R. B., Shaya, E. J., & Pierce, M. J. 1992, *ApJS*, 80, 479
- Vazdekis, A., Koleva, M., Ricciardelli, E., Röck, B., & Falcón-Barroso, J. 2016, *MNRAS*, 463, 3409
- Virtanen, P., Gommers, R., Oliphant, T. E., et al. 2020, *Nature Methods*, 17, 261
- Wake, D. A., Bundy, K., Diamond-Stanic, A. M., et al. 2017, *AJ*, 154, 86
- Walter, F., Bolatto, A. D., Leroy, A. K., et al. 2017, *ApJ*, 835, 265
- Weilbacher, P. M., Palsa, R., Streicher, O., et al. 2020, *A&A*, 641, A28
- Westmoquette, M. S., Smith, L. J., & Gallagher, J. S., I. 2011, *MNRAS*, 414, 3719
- Willick, J. A., Courteau, S., Faber, S. M., et al. 1997, *ApJS*, 109, 333
- Xilouris, E. M., Byun, Y. I., Kylařis, N. D., Paleologou, E. V., & Papamastorakis, J. 1999, *A&A*, 344, 868
- Yao, P. Z. & Quataert, E. 2023, *ApJ*, 957, 30
- ¹³ Department of Physics and Astronomy, The Johns Hopkins University, Baltimore, MD 21218, USA;
- ¹⁴ Dipartimento di Fisica e Astronomia ‘G. Galilei’, Università di Padova, Vicolo dell’Osservatorio 3, I-35122 Padova, Italy;
- ¹⁵ Argelander-Institut für Astronomie, Universität Bonn, Auf dem Hügel 71, 53121 Bonn, Germany;
- ¹⁶ Observatories of the Carnegie Institution for Science, 813 Santa Barbara Street, Pasadena, CA 91101, USA;
- ¹⁷ Departamento de Astronomía, Universidad de Chile, Camino del Observatorio 1515, Las Condes, Santiago, Chile;
- ¹⁸ Department of Astronomy, University of Maryland, College Park, MD 20742, U.S.A.;
- ¹⁹ Department of Physics and Astronomy, University of Wyoming, Laramie, WY 82071, USA;
- ²⁰ Instituto de Astronomía, Universidad Nacional Autónoma de México, Ap. 70-264, 04510 CDMX, Mexico;
- ²¹ Department of Physics, University of Connecticut, 196A Auditorium Road, Storrs, CT 06269, USA;
- ²² Universität Heidelberg, Zentrum für Astronomie, Institut für Theoretische Astrophysik, Albert-Ueberle-Str. 2, 69120 Heidelberg, Germany;
- ²³ Universität Heidelberg, Interdisziplinäres Zentrum für Wissenschaftliches Rechnen, Im Neuenheimer Feld 225, 69120 Heidelberg, Germany;
- ²⁴ Harvard-Smithsonian Center for Astrophysics, 60 Garden Street, Cambridge, MA 02138, U.S.A.;
- ²⁵ Elizabeth S. and Richard M. Cashin Fellow at the Radcliffe Institute for Advanced Studies at Harvard University, 10 Garden Street, Cambridge, MA 02138, U.S.A.;
- ²⁶ Max-Planck-Institut für Astronomie, Königstuhl 17, D-69117, Heidelberg, Germany;
- ²⁷ Sub-department of Astrophysics, Department of Physics, University of Oxford, Keble Road, Oxford OX1 3RH, UK; .

¹ European Southern Observatory (ESO), Alonso de Córdova 3107, Casilla 19, Santiago 19001, Chile;

² Astronomisches Rechen-Institut, Zentrum für Astronomie der Universität Heidelberg, Mönchhofstraße 12-14, 69120 Heidelberg, Germany;

³ Department of Astronomy, The Ohio State University, 140 West 18th Avenue, Columbus, OH 43210, USA;

⁴ Center for Cosmology and Astroparticle Physics, 191 West Woodruff Avenue, Columbus, OH 43210, USA;

⁵ European Southern Observatory, Karl-Schwarzschild Straße 2, D-85748 Garching bei München, Germany;

⁶ Univ Lyon, Univ Lyon1, ENS de Lyon, CNRS, Centre de Recherche Astrophysique de Lyon UMR5574, F-69230 Saint-Genis-Laval France;

⁷ INAF – Osservatorio Astrofisico di Arcetri, Largo E. Fermi 5, I-50157 Firenze, Italy;

⁸ Finnish Centre for Astronomy with ESO, (FINCA), University of Turku, FI-20014 Turku, Finland;

⁹ Tuorla Observatory, Department of Physics and Astronomy, University of Turku, FI-20014 Turku, Finland;

¹⁰ Turku Collegium for Science, Medicine and Technology, University of Turku, FI-20014 Turku, Finland;

¹¹ Space Telescope Science Institute, 3700 San Martin Drive, Baltimore, MD 21218, USA;

¹² International Centre for Radio Astronomy Research, University of Western Australia, 7 Fairway, Crawley, 6009 WA, Australia;

Appendix A: DAOFIND based PNLF

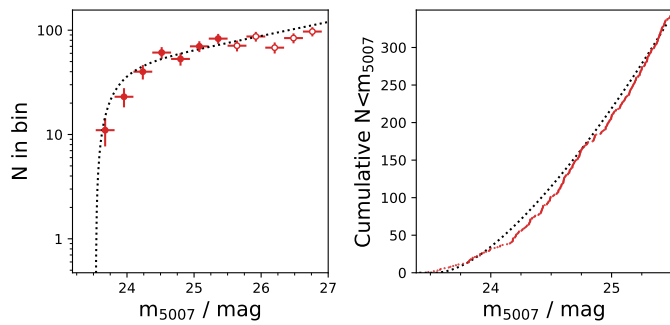


Fig. A.1. PNLF and cumulative luminosity function for NGC 253 using the sample of PNe recovered by DAOFIND. Panels, markers and colours as in Fig. 6.

In this section we repeat the selection of the PNe candidates using the well-known point source detection algorithm DAOFIND (Stetson 1987). We apply the algorithm in the version included in the `photutils` package on the $[\text{O III}]\lambda 5007$ emission line map. We used default arguments for the detection and assume a PSF size of 1 arcsec. This detection approach returns a catalogue of 10635 PNe candidates. We then processed the catalogue of PNe candidates following the procedures described in Sec. 3 to measure the FWHM of each source, the line fluxes, and to remove contaminants from the sample. The final number of confirmed PNe is 5494, a rather high number compared to what identified in the emission line maps with the detection method described in Sec. 3.1. In fact, a visual inspection of the new candidates reveals that the vast majority of them are probably false detections. However, if we consider only sources with $m_{[\text{O III}]} \leq 25.5$ mag, the number decreases to 343, quite comparable to the 319 PNe that result from visual inspection. Matching the two catalogues, we see that 309 of the 320 confirmed PNe brighter than 25.5 mag are included in the clean sample of bright PNe from DAOFIND.

We used this clean sample of bright PNe to fit the PNLF (see Fig. A.1). As expected, given the similarity between the two samples, we obtain very similar results. In particular, we obtain a distance modulus of $28.07^{+0.03}_{-0.4}$ mag, which corresponds to a distance of $4.12^{+0.07}_{-0.08}$ Mpc. Although the final results of the two detection methods are similar, the large number of false detections that are classified as PNe when using the DAOFIND catalogue made us decide to rely on visual identification for the main analysis of the paper.

Appendix B: Additional tables.

Table B.1. Summary of the observations.

OB Name	Date	Program	Airmass	Seeing	Exptime	FWHM1	FWHM2
WFM-NGC-253-NW	2019-07-29	0102.B-0078(A)	1.06	0.80	1960.0	0.70	^{-a}
WFM-NGC-253-SE	2018-11-07	0102.B-0078(A)	1.07	0.85	1960.0	0.72	^{-a}
WFM-NGC253_Pri01	2021-11-27	108.2289.001	1.21	0.58	844.8	0.74	0.79
WFM-NGC253_Pri02	2021-11-30	108.2289.001	1.09	0.55	844.8	0.85	0.82
WFM-NGC253_Pri03	2021-12-07	108.2289.001	1.32	0.84	844.8	0.99	1.15
WFM-NGC253_Pri04	2021-12-28	108.2289.001	1.23	0.51	844.8	0.68	0.76
WFM-NGC253_Pri05	2021-12-29	108.2289.001	1.22	0.77	844.8	0.91	0.78
WFM-NGC253_Pri06	2022-06-29	108.2289.001	1.17	0.49	844.8	0.69	0.84
WFM-NGC253_Pri07	2022-07-02	108.2289.001	1.33	0.57	844.8	^{-b}	0.50
WFM-NGC253_Pri08	2022-07-02	108.2289.001	1.13	0.53	844.8	0.63	0.64
WFM-NGC253_Pri09	2022-07-04	108.2289.001	1.04	0.83	844.8	0.84	0.72
WFM-NGC253_Pri10	2022-08-20	108.2289.001	1.04	0.55	844.8	0.71	0.62
WFM-NGC253_Pri11	2022-08-27	108.2289.001	1.11	0.42	844.8	0.57	0.60
WFM-NGC253_Pri12	2022-08-27	108.2289.001	1.02	0.85	844.8	0.70	0.86
WFM-NGC253_Pri13	2022-08-27	108.2289.001	1.11	0.83	844.8	0.62	0.69
WFM-NGC253_Pri14	2022-09-03	108.2289.001	1.04	0.82	844.8	0.76	0.81
WFM-NGC253_Pri15	2022-09-03	108.2289.001	1.03	0.65	844.8	0.70	0.60
WFM-NGC253_Pri16	2022-09-05	108.2289.001	1.08	0.73	844.8	0.64	0.99
WFM-NGC253_Pri17	2022-09-05	108.2289.001	1.24	0.93	844.8	0.69	0.89
WFM-NGC253_Pri18	2022-09-06	108.2289.001	1.22	0.74	844.8	0.67	1.50
WFM-NGC253_Pri18	2023-01-16	108.2289.001	1.53	0.52	844.8	0.72	0.74
WFM-NGC253_Pri19	2022-09-19	108.2289.001	1.03	1.04	844.8	1.32	1.15
WFM-NGC253_Pri20	2022-09-19	108.2289.001	1.12	1.03	844.8	1.01	0.90
WFM-NGC253_Pri21	2022-09-19	108.2289.001	1.30	1.00	844.8	0.95	^{-b}
WFM-NGC253_Pri22	2022-09-20	108.2289.001	1.03	1.07	844.8	1.25	1.04
WFM-NGC253_Pri23	2022-09-20	108.2289.001	1.02	1.63	844.8	1.31	1.61
WFM-NGC253_Pri24	2022-09-21	108.2289.001	1.10	0.60	844.8	0.67	0.85
WFM-NGC253_Pri25	2022-09-22	108.2289.001	1.17	0.78	844.8	1.01	0.96
WFM-NGC253_Pri26	2022-09-22	108.2289.001	1.09	0.74	844.8	^{-b}	0.96
WFM-NGC253_Pri27	2022-09-23	108.2289.001	1.33	0.98	844.8	0.84	1.13
WFM-NGC253_Pri28	2022-09-23	108.2289.001	1.13	0.85	844.8	0.90	1.16
WFM-NGC253_Pri29	2022-09-23	108.2289.001	1.03	0.94	844.8	1.11	0.88
WFM-NGC253_Pri30	2022-09-23	108.2289.001	1.03	0.95	844.8	0.78	0.73
WFM-NGC253_Pri31	2022-09-24	108.2289.001	1.23	1.24	844.8	1.18	0.58
WFM-NGC253_Pri32	2022-09-24	108.2289.001	1.07	0.71	844.8	0.63	0.66
WFM-NGC253_Pri33	2022-09-24	108.2289.001	1.21	0.60	844.8	0.56	0.64
WFM-NGC253_Pri34	2022-09-25	108.2289.001	1.08	1.03	844.8	1.13	0.82
WFM-NGC253_Pri35	2022-09-25	108.2289.001	1.03	0.58	844.8	0.51	0.65
WFM-NGC253_Pri36	2022-09-26	108.2289.001	1.16	0.82	844.8	0.88	0.84
WFM-NGC253_Pri37	2022-09-26	108.2289.001	1.04	0.98	844.8	0.98	0.79
WFM-NGC253_Pri38	2022-09-26	108.2289.001	1.05	0.70	844.8	0.59	0.76
WFM-NGC253_Pri39	2022-09-29	108.2289.001	1.03	0.73	844.8	0.64	0.65
WFM-NGC253_Pri40	2022-09-30	108.2289.001	1.13	0.68	844.8	0.71	0.72
WFM-NGC253_Pri41	2022-09-30	108.2289.001	1.03	0.80	844.8	0.61	0.87
WFM-NGC253_Pri42	2022-09-30	108.2289.001	1.02	1.03	844.8	0.89	0.83
WFM-NGC253_Pri43	2022-10-28	108.2289.001	1.05	0.70	844.8	0.68	0.70
WFM-NGC253_Pri44	2022-08-26	108.2289.001	1.04	0.47	844.8	0.49	0.58
WFM-NGC253_Pri45	2022-01-04	108.2289.001	1.34	0.74	844.8	0.84	0.71
WFM-NGC253_Pri46	2022-10-28	108.2289.001	1.24	0.57	844.8	0.69	0.76
WFM-NGC253_Pri47	2022-10-30	108.2289.001	1.03	0.57	844.8	0.81	0.74
WFM-NGC253_Pri48	2022-10-30	108.2289.001	1.04	0.41	844.8	0.58	0.60
WFM-NGC253_Pri49	2022-10-30	108.2289.001	1.14	0.52	844.8	0.66	0.63
WFM-NGC253_Pri51	2023-05-30	108.2289.001	1.39	0.79	844.8	0.84	^{-a}

Notes. We report the name of the OB, the date of observation, the program ID, the average airmass of the observations, the average seeing estimated from the Paranal DIMM, the exposure time, and the average full width at half maximum (FWHM) of the point spread function (PSF) for each pointing observed in the OB as derived from the PNe in Sec. 3.2. All OBs except for WFM-NGC-253-NW, WFM-NGC-253-SE, and WFM-NGC253_Pri51, include two separate pointings (see Sec 2). The exposure time refers to the single pointing. ^(a) These OBs include only a single pointing. ^(b) No PNe in the field of view of these pointings.

Table B.2. Summary of the information included in the PNe catalogue.

Position and Morphology	
ID	Identification number
RA	Right ascension of the nebula
DEC	Declination of the nebula
deproj_dist	Deprojected distance from the nucleus of the galaxy (in arcsec)
deproj_phi	Deprojected position angle (in degrees)
FWHM	FWHM of the nebula from the Moffat fit (in arcsec)
Spectral properties	
lineid should be replaced with HEII4686, HB4861, HA6562, HEI5875 ^a , OIII5006, NII6583, SII ^b	
lineid_FLUX	Background subtracted line flux ^c in 10^{-20} erg cm ⁻² s ⁻¹
lineid_FLUX_ERR	Line flux error in 10^{-20} erg cm ⁻² s ⁻¹
lineid_FLUX_BACK	Background flux in 10^{-20} erg cm ⁻² s ⁻¹
lineid_SNR	S/N of the line
m5007	m_{5007} in magnitudes
dm5007	Error on m_{5007} in magnitudes

Notes. ^(a) The He I λ 5875 line is masked by the MUSE notch filter in the two central pointings observed with AO. ^(b) The [S II] λ 6717, 6731 fluxes were recovered from a single moment map, given the vicinity of the two lines. ^(c) Line fluxes are corrected for Milky Way extinction and aperture size, as described in Sec. 3.3

Table B.3. Wavelengths and ionisation potential of the relevant ion for each emission line.

Line name	Wavelength (air) [Å]	String ID	Ionisation potential [eV]	Fixed ratio
Hydrogen Balmer lines				
H β	4861.35	HB4861	13.60	no
H α	6562.79	HA6562	13.60	no
Low ionisation lines				
[N II] λ 5197	5197.90	NI5197	—	no
[N II] λ 5200	5200.26	NI5200	—	no
[N II] λ 5754	5754.59	NII5754	14.53	no
[N II] λ 6548	6548.05	NII6548	14.53	0.34 [N II] λ 6584
[N II] λ 6584	6583.45	NII6583	14.53	no
[S II] λ 6717	6716.44	SII6716	10.36	no
[S II] λ 6731	6730.82	SII6730	10.36	no
High ionization lines				
He II λ 4686	4685.70	HEII4865	24.58	no
[O III] λ 4959	4958.91	OIII4958	35.12	0.35 [O III] λ 5007
[O III] λ 5007	5006.84	OIII5006	35.12	no
He I λ 5876	5875.61	HEI5875	—	no
[S III] λ 6312	6312.06	SIII6312	23.34	no

Notes. Wavelengths are taken from the National Institute of Standards and Technology (NIST; https://physics.nist.gov/PhysRefData/ASD/lines_form.html), and are Ritz wavelengths in air except for the H Balmer lines, in which case we use the ‘observed’ wavelength in air as reported in NIST. The DAP string name is used to identify the correct extension in the MAPS files or in the moment maps. Ionisation potentials are taken from [Draine \(2011\)](#). The [O I] lines at 6300 and 6363 Å are not included in this list because they are heavily contaminated by sky emission.

Table B.4. List of FITS extensions included in the MAPS file

Extension name	Description
Binning	
FLUX	white-light image
SNR	continuum S/N ratio for individual spaxels
SNRBIN	continuum S/N for each Voronoi bin
BIN_ID	unique ID for each Voronoi bin, unbinned spectra have bin IDs of -1
Stellar kinematics	
$\text{HN}^\#_{\text{STARS}}$ = higher order Gauss-Hermite velocity moment, if available (e.g., H3_STARS, H4_STARS)	
V_STARS	stellar velocity [km s^{-1}], after subtracting the systemic velocity
FORM_ERR_V_STARS	formal velocity error [km s^{-1}]
SIGMA_STARS	stellar velocity dispersion [km s^{-1}]
FORM_ERR_SIGMA_STARS	formal sigma error [km s^{-1}]
ERR_SIGMA_STARS	MCMC-calculated error for sigma (if available) [km s^{-1}]
$\text{HN}^\#_{\text{STARS}}$	higher order moments of the stellar LOSVD (when available)
FORM_ERR_ $\text{HN}^\#_{\text{STARS}}$	formal errors in the high-order moments
ERR_ $\text{HN}^\#_{\text{STARS}}$	MCMC errors for higher order moments (not yet available)
Stellar populations	
STELLAR_MASS_DENSITY	stellar mass surface density [$M_\odot \text{pc}^{-2}$]
STELLAR_MASS_DENSITY_ERR	error in the above [$M_\odot \text{pc}^{-2}$]
AGE_MW	$\log(\text{Age}/\text{yr})$, where the Age is mass-weighted
AGE_MW_ERR	error in the above quantity
Z_MW	mass-weighted $[Z/H]$
Z_MW_ERR	error in the above quantity
AGE_LW	$\log(\text{Age}/\text{yr})$, where the Age is luminosity-weighted (V-band)
AGE_LW_ERR	error in the above
Z_LW	luminosity-weighted (V-band) $[Z/H]$
Z_LW_ERR	error in the above quantity
EBV_STARS	$E(B - V)$ of the stellar component [mag]
Emission lines	
*emline = emission line string id listed in Table B.3	
BIN_ID_LINES	unique bin for emission lines, these are individual spaxels in the current DR2
CHI2_TOT	The χ^2 over the full fitted wavelength range.
*emline_FLUX	emission line flux [$10^{-20} \text{erg s}^{-1} \text{cm}^{-2} \text{spaxel}^{-1}$]
*emline_FLUX_ERR	emission line flux error [$10^{-20} \text{ergs}^{-1} \text{cm}^{-2} \text{spaxel}^{-1}$]
*emline_VEL	emission line velocity [km s^{-1}]
*emline_VEL_ERR	emission line velocity error [km s^{-1}]
*emline_SIGMA	emission line velocity dispersion [km s^{-1}]
*emline_SIGMA_ERR	emission line velocity dispersion error [km s^{-1}]
*emline_SIGMA_CORR	instrumental velocity dispersion at the position of the line [km s^{-1}]
*emline_MOM0	emission line moment 0 [$10^{-20} \text{erg s}^{-1} \text{cm}^{-2} \text{spaxel}^{-1}$]
*emline_MOM0_ERR	emission line moment 0 error [$10^{-20} \text{ergs}^{-1} \text{cm}^{-2} \text{spaxel}^{-1}$]
*emline_MOM1	emission moment 1 [km s^{-1}]
*emline_MOM1_ERR	emission moment 1 error [km s^{-1}]
*emline_MOM2	emission moment 2 [km s^{-1}]
*emline_MOM2_ERR	emission moment 2 error [km s^{-1}]

Notes. Each extension is a two-dimensional map on the same WCS as the mosaic datacube. We list the extension names, and a brief description of the map associated with that extension. All lines maps produced are corrected for the Milky Way foreground contribution. Moment-zero maps are not.